Orbital hydroclimate variability revealed by grain-size evidence in the tropical Pacific Islands since 140 ka

Xiaojie Tang, Zhaojie Yu, Zhengyao Lu, Lina Song, Zehua Song, Christophe Colin, Giuseppe Siani, Xiaoying Kang, Fengming Chang, Franck Bassinot, et al.

Orbital hydroclimate variability revealed by grain-size evidence in the tropical Pacific Islands since 140 ka

Xiaojie Tang, Zhaojie Yu, Zhengyao Lu, Lina Song, Zehua Song, Christophe Colin, Giuseppe Siani, Xiaoying Kang, Fengming Chang, Franck Bassinot, Shiming Wan

PII: S0921-8181(24)00076-6

DOI: https://doi.org/10.1016/j.gloplacha.2024.104429

Reference: GLOBAL 104429

To appear in: *Global and Planetary Change*

Received date: 29 October 2023

Revised date: 23 March 2024

Accepted date: 26 March 2024

Please cite this article as: X. Tang, Z. Yu, Z. Lu, et al., Orbital hydroclimate variability revealed by grain-size evidence in the tropical Pacific Islands since 140 ka, *Global and Planetary Change* (2023), https://doi.org/10.1016/j.gloplacha.2024.104429

Orbital hydroclimate variability revealed by grain-size evidence in the tropical Pacific Islands since 140 ka

Xiaojie Tang[a, e], Zhaojie Yu[a, b, c, d]*, Zhengyao Lu[f], Lina Song[a], Zehua Song[a], Christophe Colin[e], Giuseppe Siani[e], Xiaoying Kang[a], Fengming Chang[a], Franck Bassinot[g], Shiming Wan[a]

[a] Key laboratory of Ocean Observation and Forecasting, Institute of Oceanology, Chinese Academy of Sciences, Qingdao 266071, China.

[b] Laboratory for Marine Geology, Qingdao Marine Science and Technology Center, Qingdao, 266237, China

[c] Center for Ocean Mega-Science, Chinese Academy of Sciences, Qingdao 266071, China.

[d] College of Earth Science and Engineering, Shandong University of Science and Technology, Qingdao 266590, China.

[e] Université Paris-Saclay, CNRS, GEOPS, 91405, Orsay, France.

[f] Department of Physical Geography and Ecosystem Science, Lund University, Lund, Sweden

[g] LSCE/IPSL, CEA-CNRS-UVSQ, Université Paris-Saclay, F-91191 Gif-sur-Yvette, France

*Corresponding author: Zhaojie Yu, yuzhaojie@qdio.ac.cn.

Abstract:

The past evolution of precipitation and atmospheric convection in the Western Pacific Warm Pool (WPWP) is critical for global climate changes but is under debate because of its forcing mechanisms. Here, we present a high temporal resolution (~156

years) grain-size record of core MD01-2385 over the last 140 kyr, in offshore northern New Guinea to reveal sediment dynamics as a proxy for precipitation changes. End-member analysis revealed that a two-endmember model was optimal. The end-member 1/end-member 2 (EM1/EM2) ratio could represent the variation in grain size and exhibited significant precessional cycles changes in phase with modelled Niño 3 SST anomaly from a global climate model transient simulation. From these data, we inferred orbital fluctuations in precipitation from tropical western Pacific islands, with general precipitation peaks during the time of perihelion at the boreal autumnal equinox (midpoint from a low to high precession index), corresponding to La Niña-like conditions and vice versa. Comparisons of our new record with published precipitation records showed that orbital precipitation changes in the WPWP are mainly dominated by El Niño-Southern Oscillation-like (ENSO-like) oscillations in the precession band, while the Intertropical Convergence Zone (ITCZ) mainly controls the distribution of precipitation over a larger spatial area.

Key words: Grain size; Western Pacific Warm Pool; Precipitation; ENSO; orbital timescales

Highlights:

(1) First high temporal resolution grain size record of sediment dynamics in Tropical Western Pacific islands

(2) This grain size record exhibits precessional changes in phase with modelled ENSO variations

(3) Precipitation and atmospheric convection in the WPWP are likely controlled by ENSO-like conditions, while the ITCZ impacts larger spatial precipitation anomalies

1. Introduction

The tropical Pacific ocean-atmosphere system could be intricately linked to global climate changes through atmospheric circulation and teleconnection at different timescales (*Medina-Elizalde and Lea*, 2005; *Medina-Elizalde et al.*, 2008; *Raddatz et*

al., 2017; *Wang and Ding*, 2008), which includes the Western Pacific Warm Pool (WPWP) and the Eastern Equatorial Pacific (EEP) (*Ford et al.*, 2015; *Ford et al.*, 2018; *Raddatz et al.*, 2017). Specifically, the WPWP, characterized by persistently warm sea surface temperature (SST) higher than 28°C (*Fu et al.*, 1994), is critical for global climate changes because of its enormous heat content and water vapour evaporation (*Neale and Slingo*, 2003; *Sardeshmukh and Hoskins*, 1988).

However, the variability in precipitation on orbital timescales is controversial. On the one hand, precipitation patterns and mechanisms are in debate. First, there is controversy over which orbital parameter dominates climate change in the region. While most records exhibit obvious precessional cycles (*Carolin et al.*, 2013; *Carolin et al.*, 2016; *Clement et al.*, 1999; *Dang et al.*, 2015; *Hollstein et al.*, 2020; *Tachikawa et al., 2011; Wu et al., 2012*), some records show significant glacial-interglacial cycles (*Pico et al.*, 2020; *Windler et al.*, 2021; *Windler et al.*, 2019) and/or obliquity cycles (*Liu et al.*, 2015; *Zhang et al.*, 2022; *Zhang et al.*, 2020b). Second, the mechanism underlying these changes is controversial. The ITCZ and ENSO-like variation influence precipitation variability in the WPWP (*Clement et al.*, 1999; *Dang et al.*, 2015; *DiNezio et al.*, 2011; *Lu et al.*, 2019; *Tachikawa et al.*, 2011). Due to their different effects and complex interactions in climate change, it is crucial to elucidate their impacts. On the other hand, the reconstruction proxy is limited. In the WPWP, the XRF scanning element ratio of sediment cores and oxygen and hydrogen isotopes of different archives (e.g., speleothem, plant wax, and foraminifera) are widely used. However, the element ratios are based on the presumption that higher rainfall results in a greater riverine runoff (e.g., *Dang et al.* (2015); *Fraser et al.* (2014); *Mohtadi et al.* (2011)) and thus increases the relative contribution of terrestrially derived elements such as iron (Fe) or titanium (Ti) in marine sediments compared with those of marine origin, mainly calcium (Ca), but Ca is influenced by marine productivity (*Mohtadi et al.*, 2022). Oxygen and hydrogen isotopes are influenced by resources, transport way and marine precipitation (*Konecky et al.*, 2016). Therefore, more

investigations are required to reconcile the discrepancies between the different records, and diverse proxies are required to provide cross-validations of reconstructions.

Grain size is widely used as a proxy for monsoons in the South China Sea (*Huang et al.*, 2011; *Wan et al.*, 2007), East China Sea (*Xiao et al.*, 2006), Arabian sea (*Caley et al.*, 2011; *Clemens et al.*, 1996), etc. Compared to oxygen and hydrogen isotope data, grain size is unaffected by marine precipitation; compared to XRF scanning element ratios, grain size is unaffected by marine productivity. In the Southeast Asian arc island area, most sediments experience a very fast source-to-sink process (*Li et al.*, 2016), making grain size potentially to be sensitive to precipitation variability. However, its application is limited in the Southeast Asian arc island area. In the Philippines, *Yu et al.* (2018) used the fine endmember to represent the variability in precipitation over the last 2.36 Myr. In New Guinea, *Aiello et al.* (2019) applied grain size to discuss the influence of tectonics, sea-level changes and precipitation with direct and simple grain size classifications instead of end-member analysis, which unmixes grain-size distributions into geologically meaningful end-members (*Prins and Weltje*, 1999).

Here, we presented a high temporal resolution grain-size record spanning the last 140 kyr from marine sediment core MD01-2385 to provide an independent construction of precipitation and atmospheric convection variability in the North Bird's Peninsula (northwest New Guinea) (Figure 1) and cross-validation with other proxies. Furthermore, we compared the grain size data with other records and simulation results for the in WPWP and EEP to reveal the different impacts of ENSO and the ITCZ.

2 Regional Setting

The climate over the tropical western Pacific islands is warm and humid throughout the year. There are different annual rainfall patterns in different areas under the combined influence of the ENSO, the ITCZ, and related monsoon systems (*Aldrian and Dwi Susanto*, 2003).

In the study area (north New Guinea, black square in Figure 1a, b), southeast winds dominate in July, and the reverse occurs in January (Figure 1a, b). Rainfall peaks in June, although this area locates on the southern side of the equator (Figure 1d). In contrast, rainfall peaks in December in the southeast Philippines (~10° N, Figure 1c). Additionally, while the ENSO system controls interannual variability and the ITCZ controls seasonal cycles, local precipitation has a different monthly response to El Niño/La Niña events. El Niño events significantly reduce precipitation from May to October in northeastern New Guinea, and from November to April in the southeastern Philippines (Figure 1c, d).

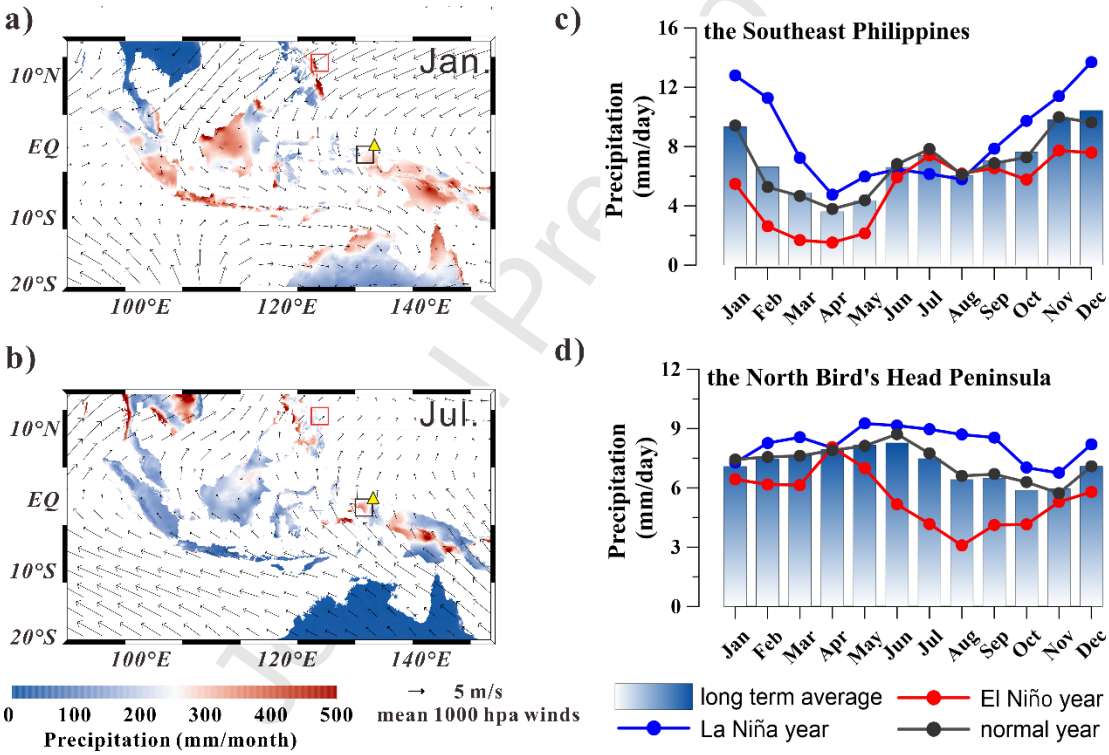

Figure 1. Modern climatology of the study region. (a, b) Mean monthly precipitation over land and mean 1000 hPa wind field in January and July. The precipitation data were obtained from http://worldclim.org and cover the period C.E. 1970-2000. The wind data were obtained from https://psl.noaa.gov/data/gridded/data.ncep.reanalysis2.html, covering C.E. 1981-2010. The yellow triangle indicates the location of core MD01-2385. (c, d) Mean monthly precipitation for the red and black boxes in (a, b), respectively, covering C.E. 1980-2020, obtained from https://downloads.psl.noaa.gov/Datasets/gpcp/; more details are provided in the supplementary

data.

Off the coast of New Guinea, strong upwelling and frontal movements are absent (*Tachikawa et al.*, 2011). Based on modern observations, the New Guinea Coastal Current (NGCC) is a seasonally reversing current in the upper 100 m, the New Guinea Coastal Under Current (NGCUC) flows northwestward throughout the year between 100 and 400 m, and both have high flow rates of up to 63 cm/s and 40 cm/s, respectively (*Kuroda*, 2000; *Wu et al.*, 2022; *Zenk et al.*, 2005; *Zhang et al.*, 2020a).

The New Guinea region is evolving within the obliquely and rapidly converging Australian and Pacific plate boundary zones (*Baldwin et al.*, 2012), thereby causing steep topography and widespread development of mafic volcanic and other metamorphic rocks (*Cloos et al.*, 2005; *Peng et al.*, 2021). In the northern Bird's Head Peninsula, the steep topography causes the emergence of many small mountain rivers, which come from the mountain as high as ~2400 m into the ocean within dozens of kilometers (Figure 2). The short transport distance and lack of fluvial plains lead to the direct transport of sediment into the sea; therefore, the grain size of the sediment is barely affected by the transport progress. The lithology (relatively young and easily weatherable basaltic rocks), topography (very steep), and climate (a tropical climate with heavy precipitation and runoff) together lead to intensive weathering and heavy sediment loads in submarine canyons and the deep sea. Specifically, the erosion rate in New Guinea reaches 1500 t/km^2/yr, and the riverine sediment fluxes reach 1200 Mt/yr in New Guinea and 140 Mt/yr in the northern Bird's Head Peninsula and Cenderawasih Bay (*Kuehl et al.*, 2004; *Milliman and Farnsworth*, 2011; *Milliman et al.*, 1999).

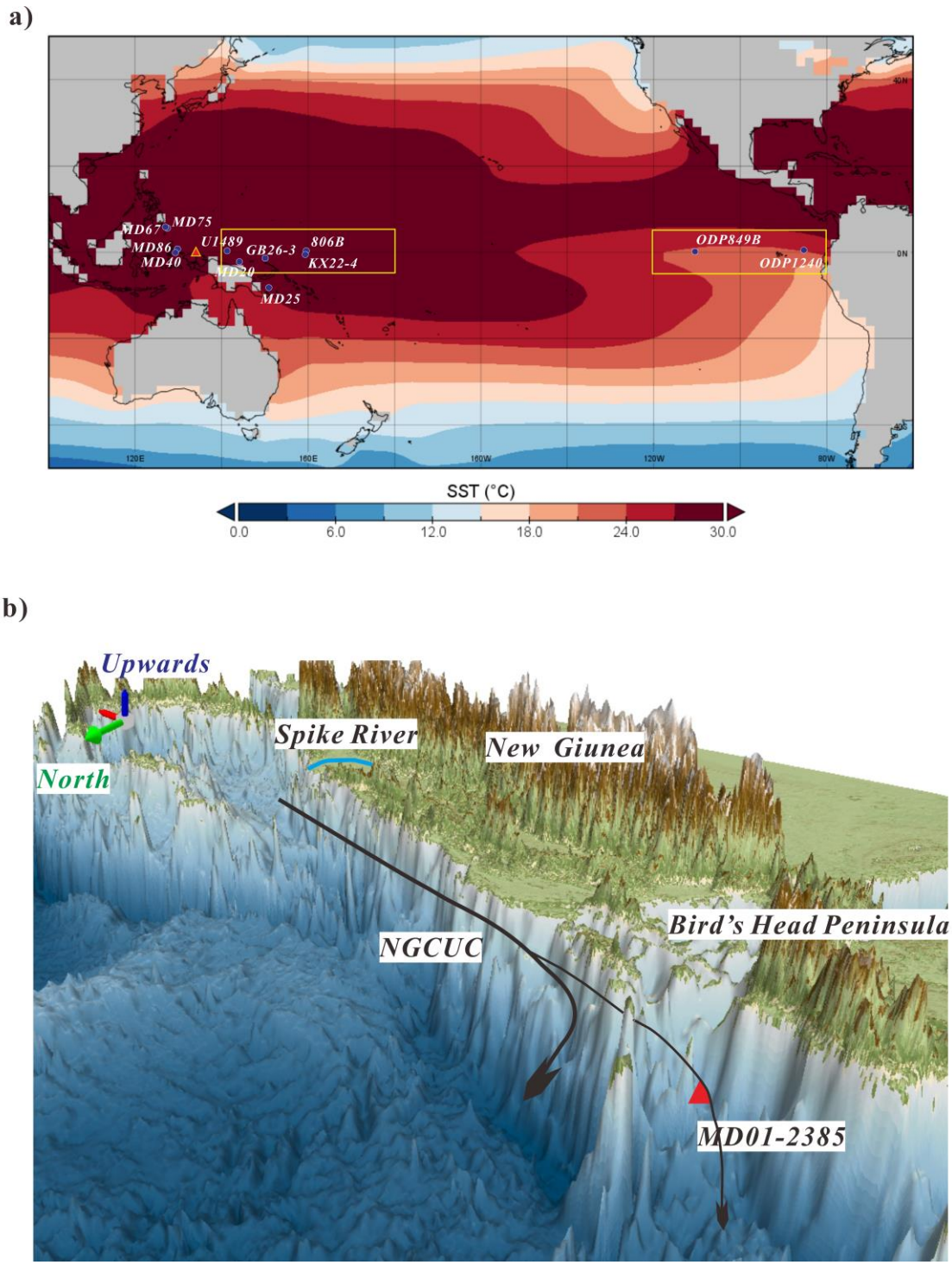

Figure 2. The regional geological and oceanological setting of the study area. (a) The modern September SST distribution with core locations mentioned in this study. (b) The bedrock map of the study area. The red triangle represents MD01-2385 (this study). MD75 is the short form for MD06-3075, MD67 for MD06-3067, MD86 for MD01-2386, MD40 for MD10-3340, GB26-3 for GeoB17426-3, MD20 for MD05-2920, and MD25 for MD05-2925. The yellow rectangles represent the "West" and "East" areas in the simulation. The blue line represents the Spike River.

The black arrows indicate the New Guinea Coastal Undercurrent (NGCUC).

3 Materials and Methods

3.1 Sediment core and age model

Sediment core MD01-2385 was collected north of Bird's Head Peninsula offshore northwest New Guinea (0.22°S, 134.24°E; water depth of 2602 m; Figure 2) during the International Marine Global Change Study (IMAGES) VII cruise conducted by the *R/V Marion Dufresne* in 2001. The lithology of this core is mainly light brown nannofossil ooze, occasionally interbedded with silty clay. No turbidites can be clearly observed in core MD01-2385. The age model is based on ten accelerator mass spectrometry (AMS) ^{14}C ages from 0 to 40 ka and five oxygen isotope stratigraphy ages from 40 to 140 ka (Figure 3). The ^{14}C ages are based on well-preserved mixed planktonic foraminifera *Globigerinoides ruber* and *Globigerinoides sacculifer* in the size fraction > 150 μm from 0 to 40 ka (*Wu et al.*, 2017; *Yu et al.*, 2023). Conventional radiocarbon ages were converted to calendar ages using Bacon and the latest calibration curve of MARINE20 (*Heaton et al.*, 2020). The local marine reservoir age ΔR was set to -108 ± 12 yr based on the mean of 5 modern measurements near MD01-2385 (*Clark et al.*, 2006; *McGregor et al.*, 2008; *Petchey and Ulm*, 2016). The oxygen isotope stratigraphy ages were established by tuning the planktonic foraminifera *G. ruber* $\delta^{18}O$ record of core MD01-2385 to the stacked *G. ruber* $\delta^{18}O$ record from nearby cores GeoB17426-3 (*Hollstein et al.*, 2020) and MD01-2386 (*Jian et al.*, 2020) because there were not enough benthic foraminifera in MD01-2385 to allow us to establish a benthic foraminifera oxygen isotopes curve. The age models for both cores (GeoB17426-3 and MD01-2386) were established by correlating their benthic foraminifera *Cibicidoides wuellerstorfi* $\delta^{18}O$ records to the LR04 benthic $\delta^{18}O$ stack (*Lisiecki and Raymo*, 2005), which can obtain a chronological model that is almost equivalent to the tuning accuracy of benthic foraminifer oxygen isotopes. Although establishing the age model by tuning the planktonic $\delta^{18}O$ record to a referenced record is widely applied in previous studies

(e.g., *Aiello et al.* (2019); *Peng et al.* (2021); *Yu et al.* (2018); *Wu et al. (*2012*)*), it is important to note that tuning with planktonic $\delta^{18}O$ record is not the preferred method for establishing the age model, rather using benthic $\delta^{18}O$ record, but unfortunately, not enough benthic foraminifera have been found in our core. Moreover, the tuning method may lead to false periodic signals that are difficult to interpret, which also require special attention. Based on this age-depth relationship, core MD01-2385 provides a continuous history from 0 to 140 ka, with an average linear sedimentation rate of 19.8 cm/kyr (ranging from 11.87 to 63.26 cm/kyr) and an average sample spacing of ~156 years.

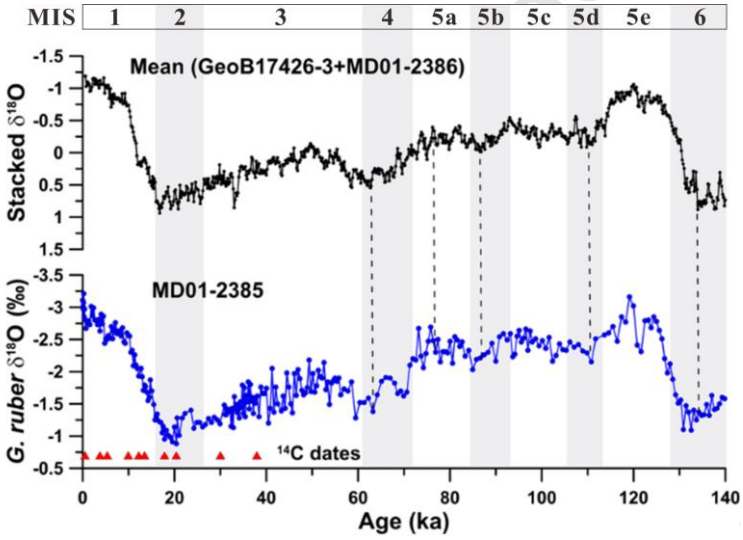

Figure 3. The age model of MD01-2385. The top diagram shows the stacked *G. ruber* $\delta^{18}O$ records from GeoB17426-3 (*Hollstein et al.*, 2020) and MD01-2386 (*Jian et al.*, 2020). The top diagram shows stacked *G. ruber* $\delta^{18}O$ records in MD01-2385. ^{14}C dating points (red triangles) are indicated at the bottom of the figure, and $\delta^{18}O$ planktonic foraminiferal tie points are linked with stacked *G. ruber* $\delta^{18}O$ records from GeoB17426-3 and MD01-2386 by dashed lines.

3.2 Grain size analysis

A total of 884 samples from core MD01-2385 were taken continuously at 2 cm intervals at 0-9 m (~70-year temporal resolution) and at 4 cm intervals (~237-year temporal resolution) at 9-27.8 m for grain-size analysis. Grain size analysis of the detrital sediments of core MD01-2385 was conducted using a Cilas 1190L Laser grain size analyser in the laboratory at the Institute of Oceanology, Chinese Academy of

Sciences (IOCAS), Qingdao. The analytical range was from 0.04 to 2500 μm. Briefly, samples were measured after the removal of carbonate and organic matter from the detrital sediments by repeatedly using excess H_2O_2 (30% at 60°C) and acetic acid (25% at 60°C), respectively (*Yu et al.*, 2018). The samples were stirred for one minute using a mechanical stirrer to mix the samples thoroughly, and 7 ml of liquid was taken at the same depth by pipette immediately after the stirring had stopped to minimise errors during sampling (*Shen et al.*, 2021). The relative standard deviations (RSD) of the repeatability and reproducibility of the instrument measurement were 0.5% and < 2%, respectively.

In this study, we applied algorithms for end-member modelling of compositional data to the grain-size distributions in core MD01-2385 (*Paterson and Heslop*, 2015). It is powerful to unmix and quantify the grain-size distributions of individual endmembers and the variations in their proportions over time (*Paterson and Heslop*, 2015; *Yu et al.*, 2018). These new algorithms, which are associated with single-specimen unmixing techniques, represent improvements over existing algorithms for addressing critical issues in identifying grain size subpopulations (*Paterson and Heslop*, 2015).

3.3 Elements Analyses

After taking the sample for grain size analysis, the samples settled for 1 hour and 22 minutes according to SediCalc to obtain the detrital clay fraction (<2 μm) from the upper 2 cm. The samples were dried at 60°C and completely dissolved before the measurement. The dilution factor was 1000. Elemental analysis was performed according to the methods of *Wan et al.* (2015). Aluminum (Al) was measured by the Varian 720es Inductively Coupled Plasma Optical Emission Spectroscopy (ICE-OES) at the wavelength of 308.215 nm. External standards included GBW07314, GBW07366, GBW07316, BHVO-2, BCR-2 for ICE-MS and ICP-OES, while the internal standard used was Re for ICP-MS. The reproducibility is ＜5% for Zr and＜ 3% for Al. ICP-MS is much more sensitive for light and trace elements compared to

XRF, and XRF is limited to surface analysis, requiring higher sample homogeneity and surface smoothness. Clay minerals are important proxies for climate changes, changes in the intensity of transport, and ocean currents (*Fagel*, 2007). Compared to bulk sediments, clay-sized sediments minimize bias from sediment sorting during transport.

3.4 National Center for Atmospheric Research-Community Climate System Model version 3 (NCAR-CCSM3) modelling

The NCAR-CCSM 3 model was employed in this work, which is fully coupled with active atmosphere, land, and ocean, sea ice components (*Otto-Bliesner et al.*, 2006; *Yeager et al.*, 2006). The ocean and sea ice models have ~3.6° longitudinal resolution and a variable latitudinal resolution (~0.9° near the equator, becomes coarser poleward), and the ocean model has 25 vertical *z* coordinate levels. We conducted a transient simulation of the past 300 kyr (*Lu et al.*, 2019). The external forcings include orbital parameters (ORB), greenhouse gases (GHG), and continental ice sheets (ICE). All model forcings were accelerated by a factor of 100; thus, 1 model year in the simulation represents real-time climate evolution over 100 years (*Lu et al.*, 2019).

We retrieved simulated West–East Pacific SST differences over the last 140 kyr to compare with proxy data. The "West" area was defined as 140~180°E, 5°S~5°N, and the "East" area was defined as 120~80°W, 5°S~5°N.

We also simulated the precipitation and moisture transport under the conditions that SS (summer solstice), AE (autumnal equinox), WS (winter solstice), and VE (vernal equinox) are at the perihelion during the last 140 kyr.

4 Results

End-member analysis (EMA) was applied to the detrital fraction of 884 grain-size samples from core MD01-2385. The goodness of fit statistics (coefficient of determination $R^2 > 0.9$, degree of specimen-median angle < 5 for two endmembers) showed that the two-endmember models were the optimised (Figure 4a-b). This two-

endmember model contained grain-size modes of 8 μm and 36 μm for end-member EM1 and EM2, respectively (Figure 4c).

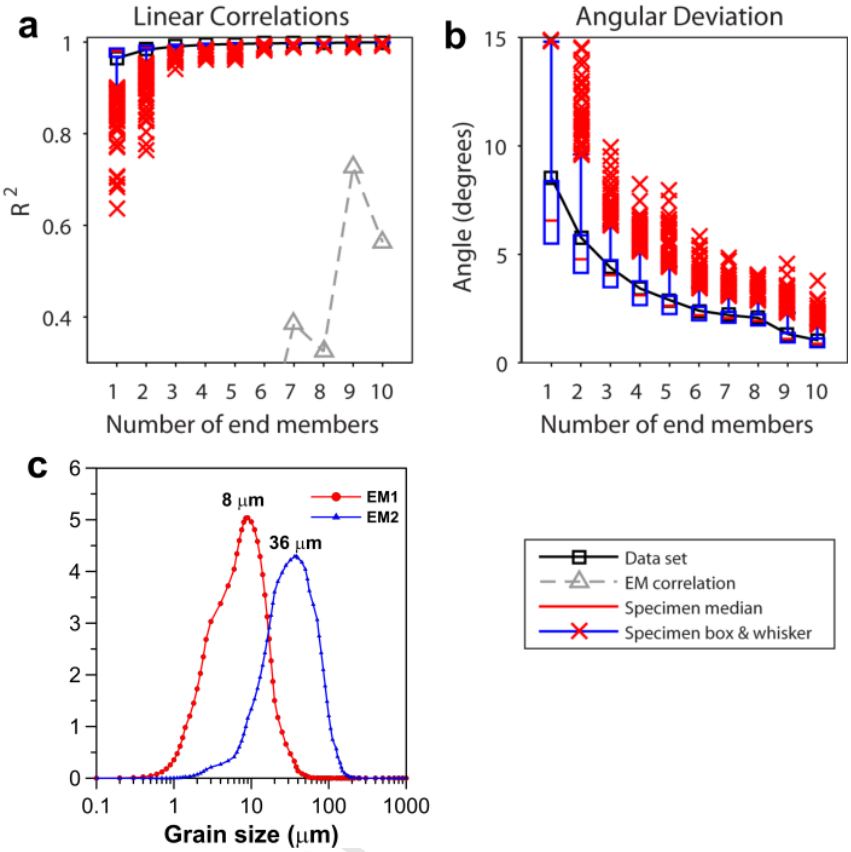

Figure 4. End-member modelling results for core MD01-2385. (a) Coefficients of determination (R^2) for each size class of models with 1–10 endmembers and (b) angular differences (in degrees) between the reconstructed and observed data sets as a function of the number of endmembers. The goodness-of-fit statistics demonstrate that the two end-member models best compromise the number of end-members and R^2 (more than 90% of the variance). (c) Modelled two endmembers of the terrigenous sediment fraction from core MD01-2385.

The proportion of EM1 varied from 52% to 100%, with an average value of 85% (Figure 5a). The change in EM2 was opposite to that in EM1, ranging between 0% and 48%, with an average value of 15%. The proportion of EM1 generally exhibited high values during interglacial MIS 1, 3, and 5. In contrast, the opposite trend was observed for the proportion of EM2 (Figure 5b). Therefore, EM1/EM2 ratios could indicate grain-size changes in detrital sediments in core MD01-2385. These ratios exhibited roughly higher values during the interglacial MIS 1, 3, and 5 and lower

values during glacial MIS 2, 4, and 6, despite an abnormally low interval during the Holocene (Figure 5c).

The value of Zr/Al varied from 5.81 to 7.76 (Figure 5e). The lowest value occurred at the end of MIS 5e and continues to increase during MIS 5d-b, and the highest value occurred during the transition between MIS 5b and 5a. After MIS 5b, there was a steep decrease and rebound in Zr/Al, and the value experienced muted variability during MIS 4-2. During MIS 1, Zr/Al decreased gradually and began to increase after 7.5 ka. The units were mg/kg and % for Zr and Al, respectively.

The W–E SST difference was simulated by NCAR-CCSM3 under the forcings of ORB, GHG, and ICE (Figure 5d). The most pronounced W–E differences occurred for MIS 5e and during the mid-Holocene. Relatively higher values were evident during MIS 5e, 5c, and 5a. At the start of MIS 4, a significant negative drift was observed, followed by a rapid increase and subsequent relatively stable conditions during MIS 3. During MIS 2, the value remained stable but lower value than that during MIS 3. A significant positive occurred during on MIS 1.

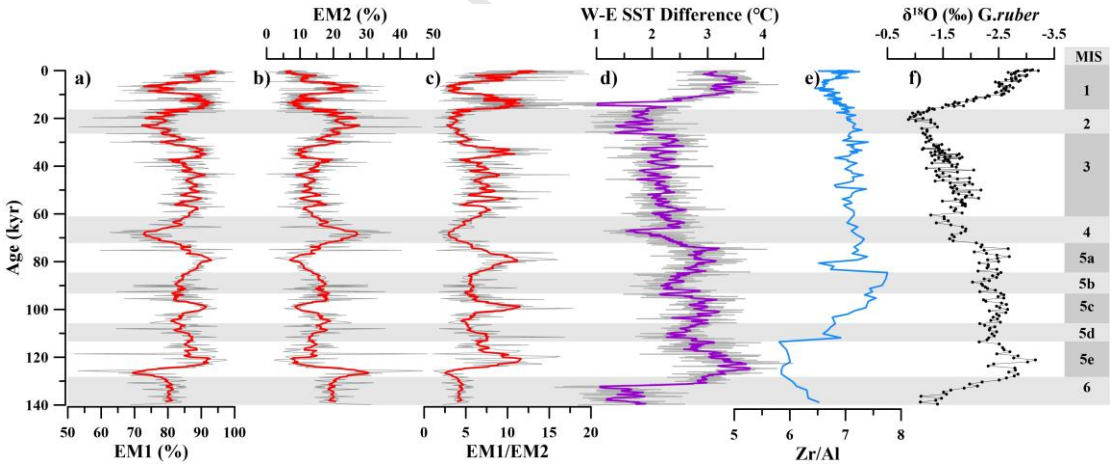

Figure 5. Relative abundances and variations in (a) grain-size endmember 1 (EM1), (b) grain-size endmember 2 (EM2), (c) EM1/EM2, (d) modelled W–E SST difference (purple line), (d) Zr/Al of the clay-size fraction (blue line), and (f) *G. ruber* $\delta^{18}O$ (black line) over the last 140 kyr. The light grey lines are the original data, and the coloured lines above are the 9-point running average in (a-d).

5 Discussion

5.1 Implications of Grain Size Variations

Core MD01-2385 is located on the northern Bird's Head Peninsula, where large amounts of fluvial sediment flow directly into the adjacent deep sea due to the extensive small mountainous rivers and narrow shelf (*Milliman*, 1995). Off the coast of northern New Guinea, riverine inputs from nearby islands are regarded as the primary source of terrigenous matter (*Aiello et al.*, 2019; *Dang et al.*, 2015; *Peng et al.*, 2021; *Tachikawa et al.*, 2011*; Wu et al., 2012*; *Yu et al.*, 2023). Additionally, there are several other possible sources, 1) aeolian dust input, 2) sediments transported by the New Guinea Coastal Current (NGCC) and New Guinea Coastal Undercurrent (NGCUC), 3) sediments transported by bottom water, and 4) sediments changes related to the sea-level and related shelf exposures.

Aeolian dust input may be an important source for the northern WPWP (*Wan et al.*, 2020; *Wan et al.*, 2012; *Yu et al.*, 2016), and is carried by westerlies and western streams (*Merrill et al.*, 1989); however, this input was considered negligible at our study site in the central WPWP because of the blockage of deep atmospheric convection (ITCZ) (*Rea et al.*, 1994). The rising branch of the atmospheric cell at the equator will obstruct the transport and sinking of the dust (*Rea et al.*, 1994). This agrees with the dust flux (lower than 0.2 $g/cm^2/yr$) in the studied area (*Wan et al.*, 2020).

The NGCC and NGCUC are the most important ocean currents in the study area. Considering the high flow rates and high riverine sediment fluxes in New Guinea, sediments from other river systems (e.g., the Spike River) outside the Bird's Head Peninsula are inevitable. However, it is unlikely that this component significantly affects our results. First, according to our results, there are two major endmembers: one is 8 μm with an average proportion of 85%, and the other is 36 μm with an average proportion of 15%. While New Guinea and North Bird's Peninsula share the same regional setting, it is unlikely that the 8 μm endmember, which took up most of the total, is transported from New Guinea (see 2 Regional Setting). Second, in New

Guinea, the depositional environment is related to the distance from the islands, i.e., a river-dominated sedimentation environment in the near-coast areas versus an ocean-dominated sedimentation environment in the "outer shelf" off the northern New Guinea with a sedimentation rate that is commonly <2~8 cm/ka (*Dang et al.*, 2020). The sediment transport pattern of the later pattern (outer shelf) is probably controlled by the NGCUC, which exhibits significant glacial-interglacial variability with enhanced sediment during glacial periods (*Dang et al.*, 2020). The sedimentation rate of MD01-2385 ranged from 11.9 to 63.3 cm/kyr, with an average value of 19.8 cm/kyr, and that of EM1/EM2 showed muted glacial cycles (Figure 6c), confirming that NGCUC is not dominant in determining the particle size or deposition processes in the study area.

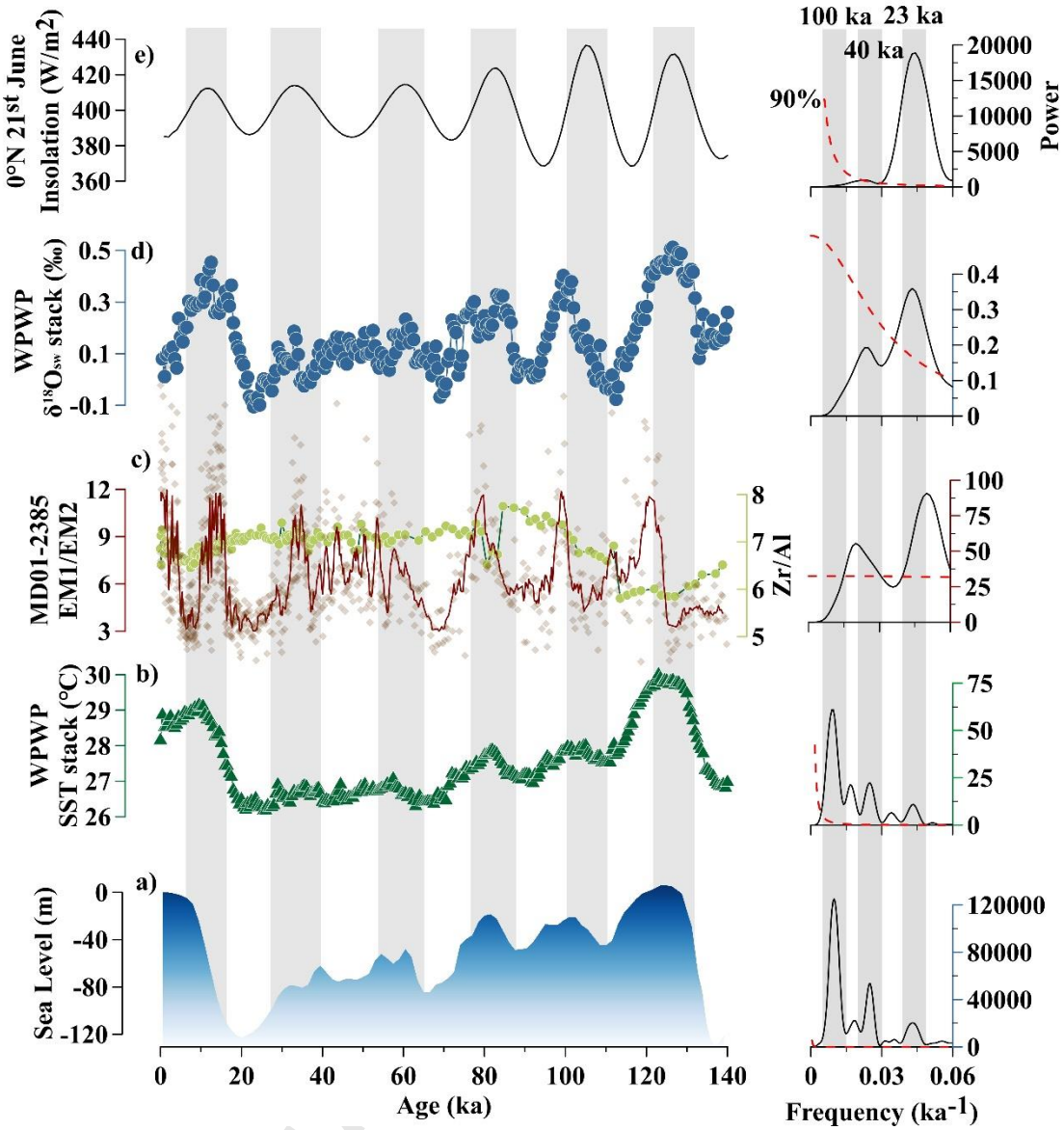

Figure 6. Comparison of reconstructed hydroclimate proxies for the WPWP, sea level, and local insolation. (a) Sea level (*Waelbroecka et al.*, 2002); (b) SST (*Jian et al.*, 2022); (c) EM1/EM2 (light red rectangle) and the Zr/Al of the clay fraction (green circle) of MD01-2385 (this study). The deep red lines represent the 7-point running average results of EM1/EM2; (d) $\delta^{18}O_{sw\text{-}iv}$ in the WPWP (*Jian et al.*, 2022); and (e) local insolation in boreal summer (*Laskar et al.*, 2004). Spectral analysis of each record (a–e) is shown on the right and was performed using the PAST software (except for Zr/Al records). The red lines are 90% confidence levels. The window function is a rectangle. The grey vertical bars mark the high insolation period on the right, and the orbital periodicities (100 ka, 40 ka, 23 ka) on the left part.

The deep water from the Southern Ocean is regarded as an important carrier of

sediments, but the unique topography around core MD01-2385 may block the northwest-flowing bottom current from MD01-2385 to some extent (Figure 2). The Zr/Al ratio also confirms this. The proxy Zr/Al indicates the accumulation of heavy minerals (e.g., zircon) over aluminosilicates under increasing bottom-current flow and is thus used as a proxy for bottom water (*Bahr et al.*, 2015; *Magill et al.*, 2018). However, the Zr/Al records show completely inconsistent changes with EM1/EM2 (Figure 6c).

We note that although we cannot completely rule out the influence of bottom water and NGCC/NGCUC, we do not consider it to be dominant in the grain-size variability in MD01-2385 on orbital timescales.

Sea level changes and related shelf exposure are considered to affect the grain size of sediment transported to the ocean (*Yu et al.*, 2019; *Zhao et al.*, 2020). On the one hand, in areas with broad shelves, most materials are deposited on these shelves (*Brunskill*, 2004; *Milliman*, 1995). On the other hand, weathering of the exposed shelf and extension of the estuarine delta may lead to changes in the chemical and physical properties of the sediment, such as that on the Sunda Shelf (*Hanebuth et al.*, 2002). However, the narrow shelf of northern New Guinea minimizes the impact of sea level in core MD01-2385. Modern measurements of the Spike River, which is on the northeast New Guinea, suggested that only 7-15% of sediments accumulate on the adjacent open shelf and slope (*Brunskill*, 2004; *Kuehl et al.*, 2004). Considering the steeper slope in the northern Bird's head peninsula, this proportion should be lower. Moreover, the exposed shelf may influence the intensity of convection here and thus affect precipitation (*DiNezio and Tierney*, 2013; *DiNezio et al.*, 2011), which may cause either a gradual shift or a jump in a proxy record due to a threshold effect on orbital timescales. However, there is no sign of a 100-kyr glacial-interglacial cycle in our record, which is excluded by the spectral analysis of EM1/EM2 (Figure 6c). During MIS 5e, Holocene, and other periods, EM1/EM2 exhibited similar amplitudes. Therefore, the results for MD01-2385, together with other nearby records (*Dang et al.*,

2020; *Tachikawa et al.*, 2011; *Yu et al.*, 2023), do not support the strong influence of sea level changes on the local climate and sediment transport.

Therefore, the riverine input from nearby islands is the primary resource for core MD01-2385 and is barely affected by sea level changes.

Temperature is an important factor for weathering (*Deng et al.*, 2022), but may not be a major factor in our case, which is similar to the conditions on the other islands of New Guinea (*Dang et al.*, 2015; *Tachikawa et al., 2011; Wu et al., 2012*; *Yu et al.*, 2023). As shown in Figure 6, EM1/EM2 in core MD01-2385 exhibited a precessional cycle similar to the hydroclimate cycle (as indicated by the stacked $\delta^{18}O_{sw\text{-}iv}$ in Figure 6d) instead of the temperature (glacial-interglacial cycles, Figure 6a and b). The spectral analysis results exhibited that both EM1/EM2 in core MD01-2385 and the stacked $\delta^{18}O_{sw\text{-}iv}$ are dominated by ~20-kyr precession cycles, while sea level and stacked SST show strong ~100-kyr eccentricity cycles (Figure 6).

In New Guinea, the erosion rate (1500 t/km^2/yr) (*Milliman*, 1995) far exceeds the supply limitation (~100 t/km^2/yr), and primary minerals are present near the surface of bedrock because the chemical weathering rate is slower than the export rate of solid matter (*West*, 2012). Under these conditions, increases in precipitation can be expected to increase both erosion rates (*Nearing et al.*, 2005) and sediment transport efficiency in the drainage basins of New Guinea (*Li et al.*, 2016; *Yu et al.*, 2023) and increase the erosion rate and cause a larger portion of EM1 (8 μm), similar to the conditions in Southwest Taiwan (*Huang et al.*, 2016; *Selvaraj and Chen*, 2006; *Wang et al.*, 2022).

Therefore, here, we use the ratio between EM1 and EM2 to indicate the physical erosion intensity, thus reflecting the precipitation variability. However, we also note that errors during sampling cannot be excluded completely, there are possible other explanations for our inferences. More modern research and simulations into the relationship between grain size and precipitation are also needed.

5.2 Comparison of precipitation proxies in the WPWP

Many investigations, most through by $\delta^{18}O_{sw\text{-}iv}$ and element ratios, into the precipitation history of the WPWP on orbital timescales have shown complex variabilities. While the element ratios records exhibited diversity (Figure 7a-e), $\delta^{18}O_{sw\text{-}iv}$ records changed more consistently (Figure 7f). The $\delta^{18}O_{sw\text{-}iv}$ record of MD01-2385 was not included because of the lack of Mg/Ca-based SST record to correct the effect of temperature.

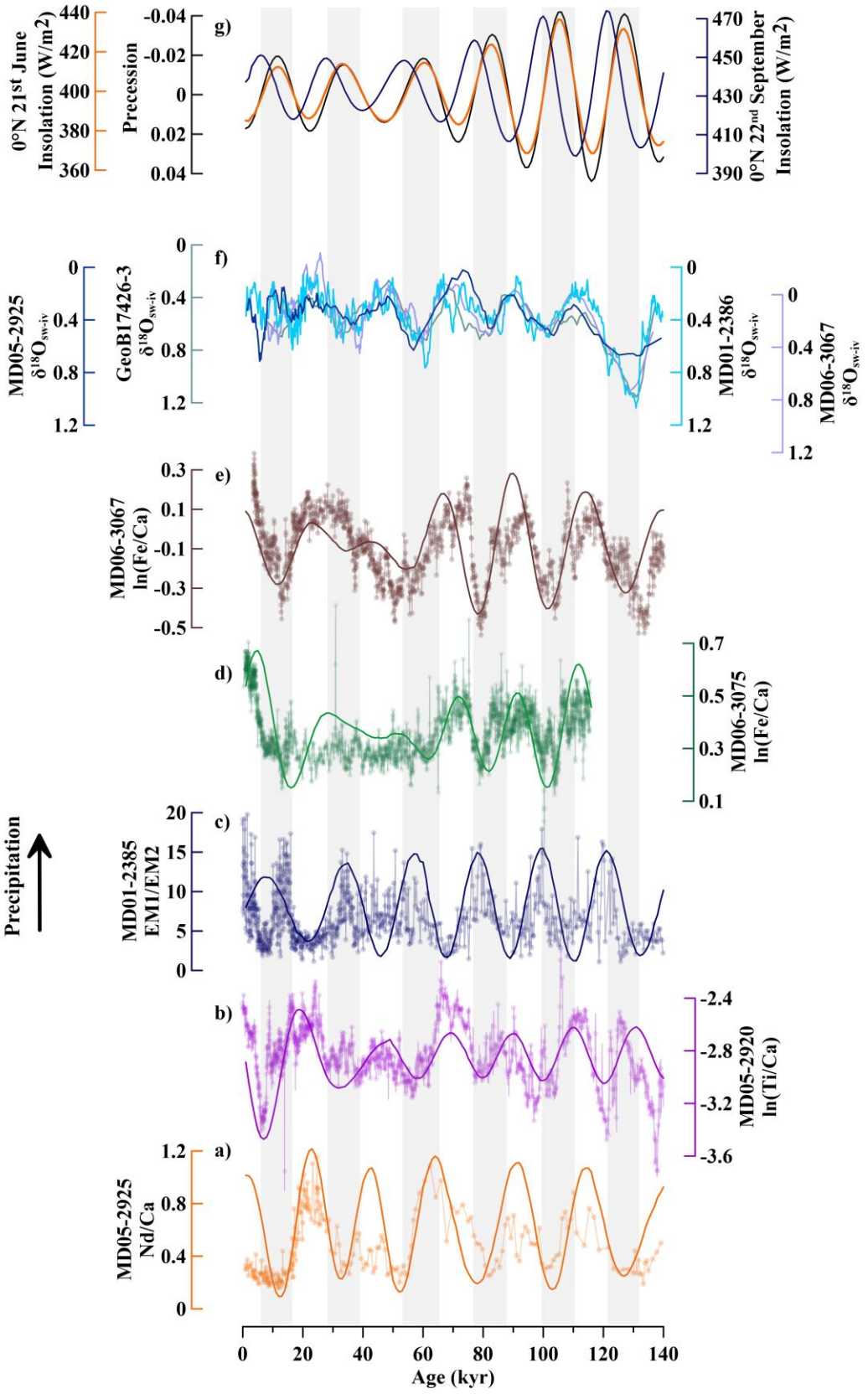

Figure 7. Different responses of different proxies. (a) Nd/Ca from MD05-2925 (*Liu et al.*, 2015).

(b) Ln(Ti/Ca) from core MD05-2920 (*Tachikawa et al.*, 2011). (c) EM1/EM2 of MD01-2385 (this study). (d) Ln(Fe/Ca) from MD06-3075 (*Fraser et al.*, 2014). (e) Ln(Fe/Ca) from MD06-3067 (*Kissel et al.*, 2010). (f) $\delta^{18}O_{sw\text{-}iv}$ records in the WPWP, which are the 7-point running averages of MD05-2925 (*Liu et al.*, 2015; *Lo et al.*, 2017), GeoB17426-3 (*Hollstein et al.*, 2020), MD01-2386 (*Jian et al.*, 2020), and MD06-3067 (*Bolliet et al.*, 2011). (g) Precession parameters and local insolation at the boreal summer solstice (21st June) and autumn equinox (22nd September) (*Laskar et al.*, 2004). The light dots in (a-e) represent the raw data, and the superimposed curves are precessional bandpass-filtered data; filtered by PAST with a central frequency of 0.043 ka^{-1} and bandwidth of 0.01 ka^{-1}, revealing differences in precipitation variability on tropical islands. (a) and (b) show typical tropical precipitation response of the Southern Hemisphere to the migration of the ITCZ; (d) and (e) are located north of the equator and change in phase with (a) and (b), but (c) located on the equator and changes anti-phase. The records in (f) show consistent changes, even at different locations. The vertical black bars indicate a lower precession period, and the upwards direction represents higher precipitation.

Multiple $\delta^{18}O_{sw\text{-}iv}$ records in WPWP exhibit similar changes in phase and amplitude under different regional settings of hydroclimate, ocean currents, etc (Figure 7) (*Fraser et al.*, 2014; *Hollstein et al.*, 2020; *Jia et al.*, 2018; *Jian et al.*, 2020; *Jian et al.*, 2022). Reconstructing precipitation through the measured $\delta^{18}O$ in calcite shells of planktic foraminifera is based on the presumption that surface ocean salinity is controlled by rainfall and freshwater input from the continent rather than by upwelling or advection through surface ocean currents, such as the semi-enclosed, nonupwelling basins off west Sumatra (*Mohtadi et al.*, 2011; *Mohtadi et al.*, 2022). The widespread currents in the WPWP and upwelling in the Philippines may cause mixing of water masses (*Fraser et al.*, 2014; *Gibbons et al.*, 2014; *Xiong et al.*, 2018). Additionally, the variability of $\delta^{18}O_{sw\text{-}iv}$ records of the WPWP may be related to the dole effect between the ocean and continent (*Huang et al.*, 2020). An increase in the ocean heat content in the WPWP will cause greater evaporation of the ocean and more vital precipitation on the continent, resulting in heavier $\delta^{18}O_{sw\text{-}iv}$ and lighter $\delta^{18}O_{cave}$ in

East Asia (*Jian et al.*, 2022; *Wang*, 2019). Therefore, $\delta^{18}O_{sw\text{-}iv}$ may be more applicable for large-scale hydrological cycles than local rainfall (Figure 7f).

The element ratios and proxy records in the WPWP illustrate a more complex precipitation pattern (Figure 7-8). Ln(Ti/Ca) and ln(Fe/Ca) are widely used as precipitation proxies. It is based on that increasing precipitation will increase the relative contribution of terrestrially derived elements, such as Fe or Ti, in marine sediments compared with those of marine origin, mainly Ca (*Mohtadi et al.*, 2022). Foraminiferal Nd/Ca was applied to precipitation reconstructions in New Guinea based on a similar theory (*Liu et al.*, 2015). Ocean current and dust input may impact Ti, Fe, and Nd, but these factors are more limited compared with riverine input in the applied cores. Therefore, they can be used as indicators of precipitation. In the WPWP, records in the southern hemisphere (MD05-2920 and MD05-2925) and in the Philippines (MD06-3067 and MD06-3075) exhibit similar changes, revealing higher precipitation in the precessional minimum (Figure 7). However, records at the equator (MD01-2385 in this study and MD10-3340 in *Dang et al.* (2015)) change differently, revealing higher precipitation during the period of perihelion at the boreal autumnal equinox, indicating potentially different mechanisms.

Based on the above discussion, the ratios of the elements could represent the precipitation in the source area, while the $\delta^{18}O_{sw\text{-}iv}$ record mainly reflects large-scale hydroclimate cycles.

5.3 The impact of ENSO-like conditions and the ITCZ in the WPWP

As shown in Figure 8, the arrows on the phase wheel point to the tropical monthly insolation variations, which the proxy records are in phase with on the 20-kyr cycle. Records from MD01-2385, MD10-3340, and Borneo show similar responses to Niño 3 SST anomalies reported in an earlier modelling study by *Clement and Cane* (1999) (red arrows), but records from the Philippines (MD06-3075) and New Guinea (MD05-2920, MD05-2925) show different responses (blue arrows) to precessional cycles. The spatial variability in precipitation in the tropical WPWP is usually

attributed to ITCZ shifts and ENSO-like conditions. The former may cause meridional precipitation anomalies through meridional migration or expansion/contraction; the latter may cause zonal precipitation anomalies.

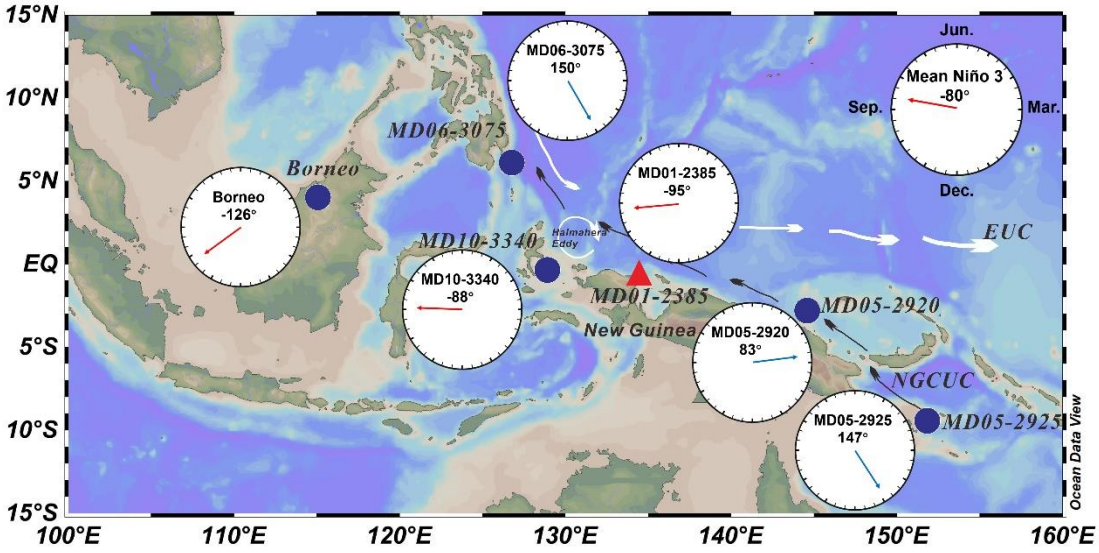

Figure 8. 20-ky period phase wheel diagrams showing the phase alignment between 0°N latitude insolation and paleoclimate reconstructions: modelled mean Niño 3 SST (*Clement and Cane*, 1999), MD05-2925 (*Liu et al.*, 2015), MD05-2920 (*Tachikawa et al.*, 2011), MD01-2385 (this study), MD06-3075 (*Fraser et al.*, 2014), MD10-3340 (*Dang et al.*, 2015), and Borneo (*Carolin et al.*, 2013; *Carolin et al.*, 2016). The degrees and arrows noted on the phase wheel indicate the phase angle between the insolation on 21st Jun of 0°N and the paleoclimate records during the 20-ky period, which were calculated by Acycle software. Note that the phase angle of speleothem $\delta^{18}O$ in Borneo is reversed by 180° because a more negative value in speleothem $\delta^{18}O$ usually indicates increasing precipitation.

The precipitation variability caused by the migration of the ITCZ and related monsoon systems is widely acknowledged in the tropical WPWP, which causes precipitation changes to follow the "seesaw pattern", that is, precipitation changes antiphases in the hemispheres (*Kutzbach et al.*, 2007; *Leduc et al.*, 2009; *Tachikawa et al.*, 2011; *Yu et al.*, 2023). However, orbital precipitation records in the WPWP do not support such seesaw patterns or mechanisms (Figure 7-8). First, the locations of MD06-3075 (6.48°N, 125.83°E) and MD05-2925 (9.35°S, 151.47°E) were considered. Their similarity cannot be attributed to the migration of the ITCZ because such drastic

swings in the position of the ITCZ appear to be unlikely from a physical point of view even on orbital timescales (*Hollstein et al.*, 2020). Second, according to modern observations, a 1° northwards shift in the zonal average precipitation centre can cause a widely-covered positive precipitation anomaly in the WPWP, including east Philippines, but a negative precipitation anomaly in north Bird's Peninsula (*McGee et al.*, 2014) was found, which contradicts to our record and other reconstructions in southeastern Philippines (*Fraser et al.*, 2014). Additionally, investigations into the modern and millennial rainfall patterns of the WPWP also do not support an ITCZ-related precipitation anomaly in this study area or in the East Philippines (*Aldrian and Dwi Susanto*, 2003; *Yu et al.*, 2023). A previous study which suggested the dominant role of the ITCZ in determining precipitation variability in the WPWP included cores from larger spatial areas (*Leduc et al.*, 2009). The records in our study were near equator, so the influence of ITCZ may have decreased.

The contraction/expansion of the ITCZ has been discussed on orbital to multidecadal timescales (*Denniston et al.*, 2016; *Scroxton et al.*, 2017; *Singarayer et al.*, 2017; *Yan et al.*, 2015; *Zhang et al.*, 2020b). On orbital timescales, the precession minimum and maximum cause a different interhemispheric temperature gradient because of the different land–sea configurations in the northern and southern hemispheres (*Singarayer et al.*, 2017; *Zhang et al.*, 2020b). According to this hypothesis, the expansion of the ITCZ might cause increasing precipitation at the southern and northern margins and decreasing precipitation at the centre of the ITCZ during the precession minimum (higher summer insolation in boreal area), which is deduced from the core U1493 (offshore northwest Australian) and Xifeng loess (East China) (*Zhang et al.*, 2020b). However, this hypothesis contradicts to proxy reconstructions in the study area (Figure 7), in which the highest precipitation in the southern and northern parts peaks at the winter solstice perihelion (precession maximum) but the precipitation at the equator peaks at the autumn equinox perihelion (highest September insolation) (Figure 7). Therefore, the dominant influence of the

ITCZ is excluded from the study area.

According to modern observations, precipitation in the tropical WPWP is sensitive to ENSO events on interannual timescales (*Aldrian and Dwi Susanto*, 2003; *Cobb et al.*, 2007; *Dang et al.*, 2015). This sandwich-like pattern in Figure 8 agrees well with modern and millennial precipitation patterns (*Aldrian and Dwi Susanto*, 2003; *Yu et al.*, 2023). In the areas where cores MD01-2385 and MD10-3340 are located, ENSO activities can cause higher precipitation in La Niña years due to the eastward movement of the convective center, and vice versa. Modern monthly precipitation analysis of the two sites revealed that the increase in precipitation caused by La Niña events occurred mainly from June to October (Figure 1d). Modern investigations of Borneo stalagmite drip water have shown that it is sensitive to the location and strength of deep convection in the WPWP with lighter $\delta^{18}O$ (higher precipitation) during La Niña conditions (*Cobb et al.*, 2007). Moreover, monthly precipitation analysis of the southeastern Philippines showed that La Niña events causes a significant increase in rainfall from December to February (Figure 1c), which also agrees with the phase relationship of MD06-3075 on the orbital timescale (Figure 8).

On orbital timescales, the grain-size records in MD01-2385 agree well with other reconstructions of ENSO-like variations (Figure 9), indicated by the W–E SST difference and Niño 3 SST anomalies. These results and our records showed consistent responses to equatorial September solar insolation (Figure 9a, d-f). The zonal thermocline tilt is closely related to the ENSO-like variations, regulated by Bjerknes feedbacks (*Bjerknes*, 1969). The thermocline depth can be determined by comparing the SST with the thermocline water temperature (TWT). Therefore, comparing the thermocline depth in the western equatorial Pacific (KX97322-4 (*Zhang et al.*, 2016; *Zhang et al.*, 2021)) to that in the eastern equatorial Pacific (ODP1240 (*Pena et al.*, 2008)) could indicate the zonal thermocline tilt (Figure 9b). A larger zonal thermocline tilt, i.e., a shoaling of thermocline depth in the EEP, is related

to intensifying upwelling, which will cause lower $\delta^{15}N$ in the EEP and higher $\Delta\delta^{15}N$ between the Western Pacific and Eastern Pacific according to modern observations (*Rafter and Charles*, 2012). The reconstructions of the zonal thermocline tilt and upwelling in the EEP are similar and show a consistent response to the variation in equatorial September insolation (Figure 9b-c). The similarity between the W–E SST difference, Niño 3 SST anomalies, zonal thermocline tilt, and upwelling reconstruction with our records supports the idea that the precipitation in North's bird Peninsula could be dominated by the ENSO-like variations on orbital timescales.

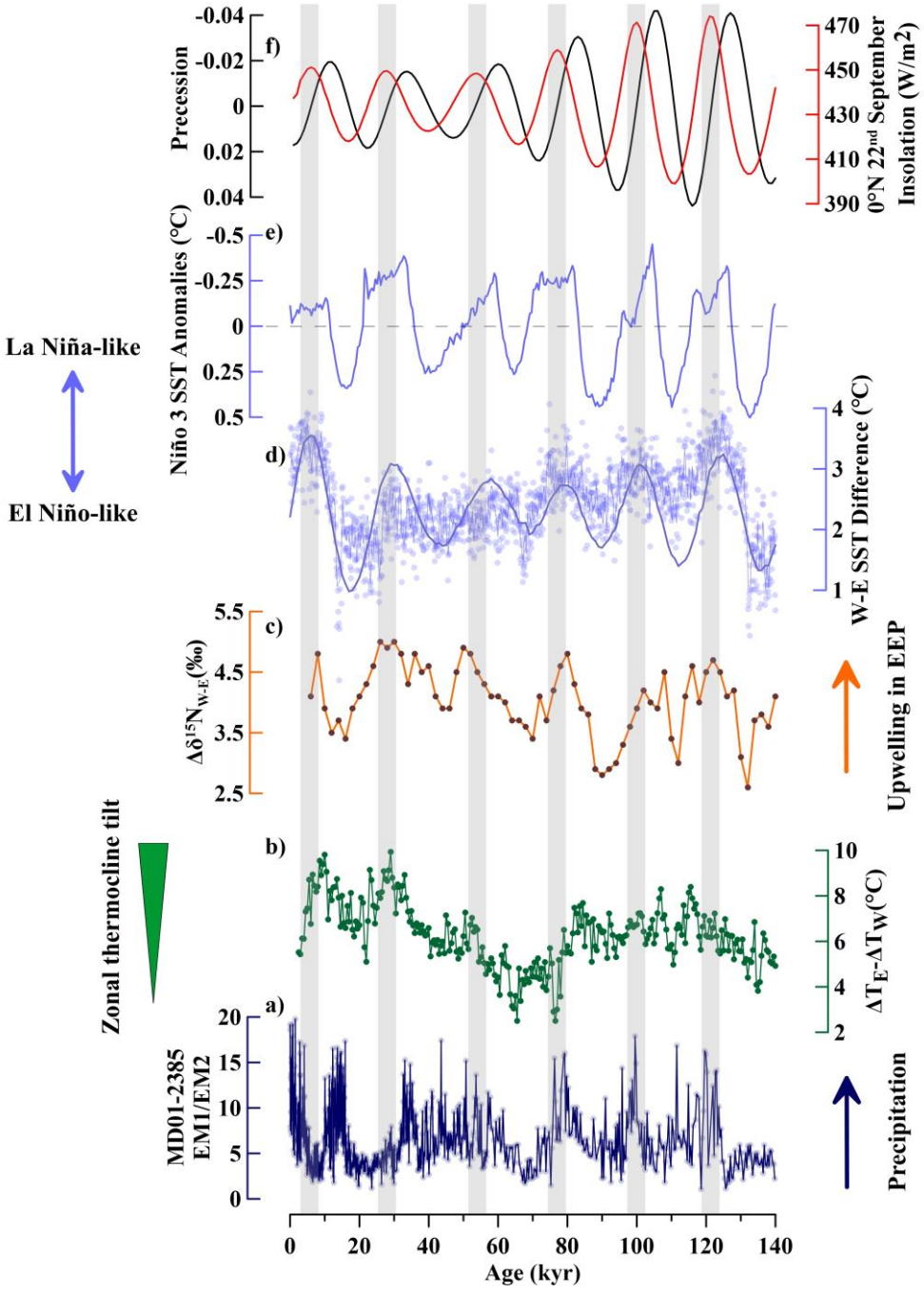

Figure 9. Comparison between grain-size records in MD01-2385 and other reconstructions of the ENSO-like variations. (a) Grain size records of MD01-2385 (this study). (b) The zonal thermocline tilt changes indicated by ΔT_E-ΔT_W *(Zhang et al., 2021)*, i.e., the comparison of the SST (*G. ruber*) minus the TWT (*N. dutertrei*) between the Eastern Pacific (ODP1240 (*Pena et al.*, 2008)) and the Western Pacific (KX97322-4 (*Zhang et al.*, 2016; *Zhang et al.*, 2021)). (c) Upwelling changes indicated by the $\Delta\delta^{15}N_{W\text{-}E}$, i.e., the $\delta^{15}N$ records in sediments in WEP minus in EEP (*Rafter and Charles*, 2012). (d) Modelled W–E Pacific SST difference (this study). The

"West" area is defined as 140~180°E, 5°S~5°N, and the "East" area is defined as 120~80°W, 5°S~5°N. (e) Modelled Niño 3 SST anomalies (*Clement and Cane*, 1999). The Niño 3 area refers to the region from 150°W to 90°W, 5°S to 5°N. (f) Precession parameter and local insolation during the autumn equinox (22nd September)(*Laskar et al.*, 2004). Our precipitation reconstruction agrees well with these ENSO-like variation indicators on orbital timescales. The grey dashed line in (c) represents the mean state of the ENSO-like system. The grey bars correspond to the September insolation maximum. The locations of the cores and simulation areas are illustrated in Figure 2. Note that the La Niña-like (El Niño-like) condition is a tendency towards an increasing (decreasing) W-E SST gradient in the Pacific Ocean compared to the average condition over the period of the last 140 kyr, rather than a modern condition.

The impact and mechanism of ENSO activities in the tropics have been extensively studied, with influences of orbital parameters, especially precession (*Clement and Cane*, 1999; *Clement et al.*, 1999; *Koutavas and Joanides*, 2012; *Liu et al.*, 2014; *Lu et al.*, 2019; *Timmermann et al.*, 2007; *Zhang et al.*, 2021). During March to April, the SST and wind field are nearly symmetric about the equator, and cold tongues in the Eastern Pacific are almost absent (*Mitchell and Wallace*, 1992). With the onset of the summer monsoon (from May to June), northwards cross-equatorial winds strengthen over the Eastern Pacific, and cold tongues reappear (*Mitchell and Wallace*, 1992). Increased northwards flow induces upwelling and surface cooling south of the equator; in turn, this cooling enhances the meridional and zonal pressure-gradient forces, further intensifying meridional and zonal wind flow, both of which promote upwelling and sustain the cold tongue (*Mitchell and Wallace*, 1992). This asymmetry in the cold tongue-ITCZ complex in EEP is regarded to be ultimately related to the hemispheric land ratio and continental geometry and be further amplified by ocean-atmosphere interactions (*Philander et al.*, 1996). The cold tongue-ITCZ complex persists through September (*Philander et al.*, 1996), while the wind field in the Western Pacific is relatively convergent, which means that the heating of the atmosphere in the WPWP is larger than that in the EEP (*Clement et al.*,

1999)(Figure 2). This zonal asymmetry in the atmospheric heating anomaly drives the easterly wind anomalies at the equator and is thought to be a primary forcing for the development of ENSO (*Clement et al.*, 1999). On the orbital timescale, the increased insolation at the equator (more effective radiative forcing in the western Pacific than the eastern Pacific) from September to October would also enhance latitudinal wind-field asymmetry and easterly wind anomalies, and cause more equatorial upwelling (Figure 9c) and shoaling of the thermocline in the eastern equatorial Pacific (Figure 9d), pushing the convective centre westwards (more precipitation in MD01-2385), and giving rise to La Niña conditions, and vice versa (Figure 9b-c) (*Carolin et al.*, 2016; *Clement et al.*, 1999; *Dang et al.*, 2015).

The simulation results further confirmed that the precipitation in the WPWP is strongest when the equatorial September insolation is at its maximum (Figure 10), corresponding to the autumnal equinox perihelion. In Figure 10, the VE (Vernal Equinox) is chosen as the benchmark and compared with WS (Winter Solstice), SS (Summer Solstice), and AE (Autumnal Equinox) as VE shows the lowest annual average precipitation. Each condition is a composite of the last 6 cases (in precession cycles) during the last 140 kyr. The results show the largest annual rainfall and moisture convergence over the MD01-2385 region at VE rather than SS in WPWP (Figure 10), which is consistent with our reconstruction and the record from core MD10-3340 (Dang et al., 2015). However, the response of rainfall variation in the Philippines and New Guinea is relatively less significant in the simulation results.

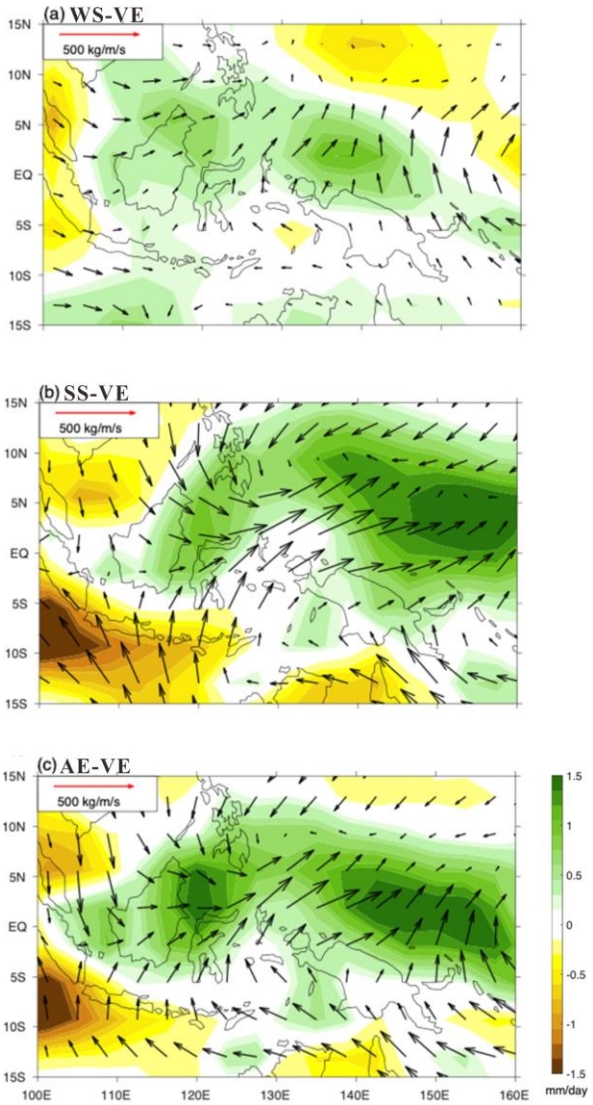

Figure 10. The simulated annual mean precipitation (shading) and vertically integrated moisture transport (vectors) are depicted by vectors in the context of six composite cases over the last 140 ka. (a) WS-VE (winter solstice-vernal equinox), (b) SS-VE (summer solstice-vernal equinox). (c) AE-VE (autumnal equinox-vernal equinox).

We are aware that the ENSO-like system is complex and the exact response phase and event intensity may be influenced by the annual cycle of the clouds and the Southern Ocean (*Lu et al.*, 2019; *Timmermann et al.*, 2007; *Zhang et al.*, 2021; *Zhang et al.*, 2023), etc. Additionally, the ITCZ may be dominant in a larger region (*Leduc et al.*, 2009). We note that the impact of the ENSO-like system is not constrained in this area and may have a global impact through teleconnection (*Jian et al.*, 2022; *Katherine et al.*, 2003; *Wang*, 2021). More investigations are needed on the ENSO-

like system and ITCZ.

6. Conclusion

Through grain-size analyses and end-member modelling, the detrital sediment from core MD01-2385 collected off northern New Guinea was depicted using a mixture of two end-members over the last 140 kyr. Considering the weathering-limited conditions in New Guinea and the relatively single sediment provenance, the EM1/EM2 ratio represents the intensity of physical erosion, which varies over time corresponding to local precipitation and deep convection in the WPWP.

Compared with other precipitation reconstructions, the EM1/EM2 ratios change differently from the northern cores (MD06-3075 and MD06-3067) and southern cores (MD05-2920 and MD05-2925). This special sandwich-like pattern excludes the possibility of a dominant role of the ITCZ regardless of the migration hypothesis or contraction/expansion hypothesis.

The precipitation variability may be dominated by the ENSO-like conditions on orbital timescales, as indicated by similar variations between EM1/EM2 records and modeled SST results, zonal thermocline tilt reconstruction, and upwelling reconstruction in the EEP. A higher EM1/EM2 coincides with La Niña-like condition, showing that La Niña-like conditions bring more precipitation to the study area and vice versa. Therefore, the precipitation and atmospheric convection in the equatorial WPWP may be dominated by the ENSO-like variations, while the ITCZ may dominate the meridional precipitation in a large spatial area.

Acknowledgement

We thank the IPEV (Institut Polaire Emile Victor), the crews, and the scientific teams of the IMAGES VII Cruise 2001 for their excellent work during core sampling. This study was supported by the Strategic Priority Research Program of the Chinese Academy of Sciences (XDB42010402), the National Natural Science Foundation of China (42376055, 91958107 and 42176034), the Natural Science Foundation of Shandong (ZR2022YQ33), Youth Innovation Promotion Association, CAS (2020210).

References

Aiello, I. W., Bova, S. C., Holbourn, A. E., Kulhanek, D. K., Ravelo, A. C., and Rosenthal, Y. (2019), Climate, sea level and tectonic controls on sediment discharge from the Sepik River, Papua New Guinea during the Mid- to Late Pleistocene, *Marine Geology*, *415*, 105954.

Aldrian, E., and Dwi Susanto, R. (2003), Identification of three dominant rainfall regions within Indonesia and their relationship to sea surface temperature, *International Journal of Climatology*, *23*(12), 1435-1452.

Bahr, A., et al. (2015), Persistent monsoonal forcing of Mediterranean Outflow Water dynamics during the late Pleistocene, *Geology*, *43*(11), 951-954.

Baldwin, S. L., Fitzgerald, P. G., and Webb, L. E. (2012), Tectonics of the New Guinea Region, *Annual Review of Earth and Planetary Sciences*, *40*(1), 495-520.

Bjerknes, J. (1969), Atmospheric Teleconnections from the Equatorial Pacific1, *Monthly Weather Review*, *97*(3), 163-172.

Bolliet, T., Holbourn, A., Kuhnt, W., Laj, C., Kissel, C., Beaufort, L., Kienast, M., Andersen, N., and Garbe-Schönberg, D. (2011), Mindanao Dome variability over the last 160 kyr: Episodic glacial cooling of the West Pacific Warm Pool, *Paleoceanography*, *26*(1).

Brunskill, G. J. (2004), New Guinea and its coastal seas, a testable model of wet tropical coastal processes: an introduction to Project TROPICS, *Continental Shelf Research*, *24*(19), 2273-2295.

Caley, T., Malaizé, B., Zaragosi, S., Rossignol, L., Bourget, J., Eynaud, F., Martinez, P., Giraudeau, J., Charlier, K., and Ellouz-Zimmermann, N. (2011), New Arabian Sea records help decipher orbital timing of Indo-Asian monsoon, *Earth and Planetary Science Letters*, *308*(3-4), 433-444.

Carolin, S. A., Cobb, K. M., Adkins, J. F., Clark, B., Conroy, J. L., Lejau, S., Malang, J., and Tuen, A. A. (2013), Varied response of western Pacific hydrology to climate forcings over the last glacial period, *Science*, *340*(6140), 1564-1566.

Carolin, S. A., Cobb, K. M., Lynch-Stieglitz, J., Moerman, J. W., Partin, J. W., Lejau, S., Malang, J., Clark, B., Tuen, A. A., and Adkins, J. F. (2016), Northern Borneo stalagmite records reveal West Pacific hydroclimate across MIS 5 and 6, *Earth and Planetary Science Letters*, *439*, 182-193.

Clark, G., Anderson, A., and Wright, D. (2006), Human Colonization of the Palau Islands, Western Micronesia, *The Journal of Island and Coastal Archaeology*, *1*(2), 215-232.

Clemens, S. C., Murray, D. W., and Prell, W. L. (1996), Nonstationary Phase of the Plio-Pleistocene Asian Monsoon, *Science*, *274*(5289), 943-948.

Clement, A. C., and Cane, M. (1999), A Role for the Tropical Pacific Coupled Ocean-

Atmosphere System on Milankovitch and Millennial Timescales. Part I: A Modeling Study of Tropical Pacific Variability, in *Mechanisms of Global Climate Change at Millennial Time Scales*, edited by P. U. Clark, R. S. Webb and L. D. Keiwin, pp. 363-371, AGU, Washington, D. C.

Clement, A. C., Seager, R., and Cane, M. A. (1999), Orbital controls on the El Niño/Southern Oscillation and the tropical climate, *Paleoceanography*, *14*(4), 441-456.

Cloos, M., Sapiie, B., Quarles van Ufford, A., Weiland, R. J., Warren, P. Q., and McMahon, T. P. (2005), Collisional delamination in New Guinea: The geotectonics of subducting slab breakoff, edited, pp. 1-51, Geological Society of America Special Paper.

Cobb, K. M., Adkins, J. F., Partin, J. W., and Clark, B. (2007), Regional-scale climate influences on temporal variations of rainwater and cave dripwater oxygen isotopes in northern Borneo, *Earth and Planetary Science Letters*, *263*(3-4), 207-220.

Dang, H., Jian, Z., Kissel, C., and Bassinot, F. (2015), Precessional changes in the western equatorial Pacific Hydroclimate: A 240 kyr marine record from the Halmahera Sea, East Indonesia, *Geochemistry, Geophysics, Geosystems*, *16*(1), 148-164.

Dang, H., Wu, J., Xiong, Z., Qiao, P., Li, T., and Jian, Z. (2020), Orbital and sea-level changes regulate the iron-associated sediment supplies from Papua New Guinea to the equatorial Pacific, *Quaternary Science Reviews*, *239*, 106361.

Deng, K., Yang, S., and Guo, Y. (2022), A global temperature control of silicate weathering intensity, *Nature Communications*, *13*(1), 1-10 %* 2022 The Author(s) %U https://www.nature.com/articles/s41467-41022-29415-41460.

Denniston, R. F., et al. (2016), Expansion and Contraction of the Indo-Pacific Tropical Rain Belt over the Last Three Millennia, *Scientific Reports*, *6*, 34485.

DiNezio, P. N., and Tierney, J. E. (2013), The effect of sea level on glacial Indo-Pacific climate, *Nature Geoscience*, *6*(6), 485-491.

DiNezio, P. N., Clement, A., Vecchi, G. A., Soden, B., Broccoli, A. J., Otto-Bliesner, B. L., and Braconnot, P. (2011), The response of the Walker circulation to Last Glacial Maximum forcing: Implications for detection in proxies, *Paleoceanography*, *26*(3), PA3217.

Fagel, N. (2007), Chapter Four Clay Minerals, Deep Circulation and Climate, *1*, 139-184.

Ford, H. L., Ravelo, A. C., and Polissar, P. J. (2015), Reduced El Niño–Southern Oscillation during the Last Glacial Maximum, *Science*, *347*(6219), 255-258 %U https://doi.org/210.1126/science.1258437.

Ford, H. L., McChesney, C. L., Hertzberg, J. E., and McManus, J. F. (2018), A Deep Eastern Equatorial Pacific Thermocline During the Last Glacial Maximum, *Geophysical Research Letters*, *45*(21).

Fraser, N., Kuhnt, W., Holbourn, A., Bolliet, T., Andersen, N., Blanz, T., and Beaufort,

L. (2014), Precipitation variability within the West Pacific Warm Pool over the past 120 ka: Evidence from the Davao Gulf, southern Philippines, *Paleoceanography*, *29*(11), 1094-1110.

Fu, R., Del Genio, A. D., and Rossow, W. B. (1994), Influence of Ocean Surface Conditions on Atmospheric Vertical Thermodynamic Structure and Deep Convection, *Journal of Climate*, *7*(7), 1092-1108.

Gibbons, F. T., Oppo, D. W., Mohtadi, M., Rosenthal, Y., Cheng, J., Liu, Z., and Linsley, B. K. (2014), Deglacial δ18O and hydrologic variability in the tropical Pacific and Indian Oceans, *Earth and Planetary Science Letters*, *387*(2014), 240-251.

Hanebuth, T., Stattegger, K., and Saito, Y. (2002), The stratigraphic architecture of the central Sunda Shelf (SE Asia) recorded by shallow-seismic surveying, *Geo-Marine Letters*, *22*(2), 86-94.

Heaton, T. J., et al. (2020), Marine20—The Marine Radiocarbon Age Calibration Curve (0–55,000 cal BP), *Radiocarbon*, *62*(4), 779–820.

Hollstein, M., Mohtadi, M., Kienast, M., Rosenthal, Y., Groeneveld, J., Oppo, D. W., Southon, J. R., and Lückge, A. (2020), The Impact of Astronomical Forcing on Surface and Thermocline Variability Within the Western Pacific Warm Pool Over the Past 160 kyr, *Paleoceanography and Paleoclimatology*, *35*(6), e2019PA003832.

Hollstein, M., Mohtadi, M., Rosenthal, Y., Prange, M., Oppo, D. W., Martínez Méndez, G., Tachikawa, K., Moffa Sanchez, P., Steinke, S., and Hebbeln, D. (2018), Variations in Western Pacific Warm Pool surface and thermocline conditions over the past 110,000 years: Forcing mechanisms and implications for the glacial Walker circulation, *Quaternary Science Reviews*, *201*, 429-445.

Huang, E., Wang, P., Wang, Y., Yan, M., Tian, J., Li, S., and Ma, W. (2020), Dole effect as a measurement of the low-latitude hydrological cycle over the past 800 ka, *Science Advances*, *6*(41), eaba4823.

Huang, J., Li, A., and Wan, S. (2011), Sensitive grain-size records of Holocene East Asian summer monsoon in sediments of northern South China Sea slope, *Quaternary Research*, *75*(3), 734-744.

Huang, J., Wan, S., Xiong, Z., Zhao, D., Liu, X., Li, A., and Li, T. (2016), Geochemical records of Taiwan-sourced sediments in the South China Sea linked to Holocene climate changes, *Palaeogeography, Palaeoclimatology, Palaeoecology*, *441*, 871-881.

Jia, Q., Li, T., Xiong, Z., Steinke, S., Jiang, F., Chang, F., and Qin, B. (2018), Hydrological variability in the western tropical Pacific over the past 700kyr and its linkage to Northern Hemisphere climatic change, *Palaeogeography, Palaeoclimatology, Palaeoecology*, *493*, 44-54.

Jian, Z., Wang, Y., Dang, H., Lea, D. W., Liu, Z., Jin, H., and Yin, Y. (2020), Half-precessional cycle of thermocline temperature in the western equatorial Pacific and its bihemispheric dynamics, *Proceedings of the National Academy of*

Sciences, *117*(13), 7044-7051.

Jian, Z., et al. (2022), Warm pool ocean heat content regulates ocean–continent moisture transport, *Nature*, *612*(7938), 92-99.

Katherine, V., Robert, T., and Lowell, S. (2003), Magnitude and timing of temperature change in the Indo-Pacific warm pool during deglaciation, *Nature*, *421*(6919), 152-155.

Kissel, C., Laj, C., Kienast, M., Bolliet, T., Holbourn, A., Hill, P., Kuhnt, W., and Braconnot, P. (2010), Monsoon variability and deep oceanic circulation in the western equatorial Pacific over the last climatic cycle: Insights from sedimentary magnetic properties and sortable silt, *Paleoceanography*, *25*(3 %U https://onlinelibrary.wiley.com/doi/abs/10.1029/2010PA001980).

Konecky, B., Russell, J., and Bijaksana, S. (2016), Glacial aridity in central Indonesia coeval with intensified monsoon circulation, *Earth and Planetary Science Letters*, *437*, 15-24.

Koutavas, A., and Joanides, S. (2012), El Niño-Southern Oscillation extrema in the Holocene and Last Glacial Maximum, *Paleoceanography*, *27*(4), PA4208.

Kuehl, S. A., Brunskill, G. J., Burns, K., Fugate, D., Kniskern, T., and Meneghini, L. (2004), Nature of sediment dispersal off the Sepik River, Papua New Guinea: preliminary sediment budget and implications for margin processes, *Continental Shelf Research*, *24*(19), 2417-2429.

Kuroda, Y. (2000), Variability of Currents off the Northern Coast of New Guinea, *Journal of Oceanography*, *56*(1), 103-116.

Kutzbach, J. E., Liu, X., Liu, Z., and Chen, G. (2007), Simulation of the evolutionary response of global summer monsoons to orbital forcing over the past 280,000 years, *Climate Dynamics*, *30*(6), 567-579.

Lückge, A., Mohtadi, M., Rühlemann, C., Scheeder, G., Vink, A., Reinhardt, L., and Wiedicke, M. (2009), Monsoon versus ocean circulation controls on paleoenvironmental conditions off southern Sumatra during the past 300,000 years, *Paleoceanography*, *24*(1), n/a-n/a.

Laskar, J., Robutel, P., Joutel, F., Gastineau, M., Correia, A. C. M., and Levrard, B. (2004), A long-term numerical solution for the insolation quantities of the Earth, *Astronomy & Astrophysics*, *428*(1), 261-285.

Leduc, G., Vidal, L., Tachikawa, K., and Bard, E. (2009), ITCZ rather than ENSO signature for abrupt climate changes across the tropical Pacific?, *Quaternary Research*, *72*(1), 123-131.

Li, C., Yang, S., Zhao, J.-x., Dosseto, A., Bi, L., and Clark, T. R. (2016), The time scale of river sediment source-to-sink processes in East Asia, *Chemical Geology*, *446*, 138-146.

Lisiecki, L. E., and Raymo, M. E. (2005), A Pliocene-Pleistocene stack of 57 globally distributed benthic δ18O records, *Paleoceanography*, *20*(1), PA1003.

Liu, Y., et al. (2015), Obliquity pacing of the western Pacific Intertropical Convergence Zone over the past 282,000 years, *Nature Communications*, *6*,

10018.

Liu, Z., Lu, Z., Wen, X., Otto-Bliesner, B. L., Timmermann, A., and Cobb, K. M. (2014), Evolution and forcing mechanisms of El Nino over the past 21,000 years, *Nature*, *515*(7528), 550-553.

Lo, L., et al. (2017), Nonlinear climatic sensitivity to greenhouse gases over past 4 glacial/interglacial cycles, *Scientific Reports*, *7*(1), 4626.

Lu, Z., Liu, Z., Chen, G., and Guan, J. (2019), Prominent Precession Band Variance in ENSO Intensity Over the Last 300,000 Years, *Geophysical Research Letters*, *46*(16), 9786-9795.

Magill, C. R., Ausin, B., Wenk, P., McIntyre, C., Skinner, L., Martinez-Garcia, A., Hodell, D. A., Haug, G. H., Kenney, W., and Eglinton, T. I. (2018), Transient hydrodynamic effects influence organic carbon signatures in marine sediments, *Nat Commun*, *9*(1), 4690.

McGee, D., Donohoe, A., Marshall, J., and Ferreira, D. (2014), Changes in ITCZ location and cross-equatorial heat transport at the Last Glacial Maximum, Heinrich Stadial 1, and the mid-Holocene, *Earth and Planetary Science Letters*, *390*, 69-79.

McGregor, H. V., Gagan, M. K., McCulloch, M. T., Hodge, E., and Mortimer, G. (2008), Mid-Holocene variability in the marine 14C reservoir age for northern coastal Papua New Guinea, *Quaternary Geochronology*, *3*(3), 213-225.

Medina-Elizalde, M., and Lea, D. W. (2005), The mid-Pleistocene transition in the tropical Pacific, *Science*, *310*(5750), 1009-1012.

Medina-Elizalde, M., Lea, D. W., and Fantle, M. S. (2008), Implications of seawater Mg/Ca variability for Plio-Pleistocene tropical climate reconstruction, *Earth and Planetary Science Letters*, *269*(3-4), 585-595.

Merrill, J. T., Uematsu, M., and Bleck, R. (1989), Meteorological analysis of long range transport of mineral aerosols over the North Pacific, *Journal of Geophysical Research: Atmospheres*, *94*(D6), 8584-8598.

Milliman, J. D. (1995), Sediment discharge to the ocean from small mountainous rivers: The New Guinea example, *Geo-Marine Letters*, *15*(3-4), 127-133.

Milliman, J. D., and Farnsworth, K. L. (2011), *River Discharge to the Coastal Ocean: A Global Synthesis*, Cambridge University Press.

Milliman, J. D., Farnsworth, K. L., and Albertin, C. S. (1999), Flux and fate of fluvial sediments leaving large islands in the East Indies, *Journal of Sea Research*, *41*(1-2), 97-107.

Mitchell, T. P., and Wallace, J. M. (1992), The Annual Cycle in Equatorial Convection and Sea Surface Temperature, *Journal of Climate*, *5*(10), 1140-1156.

Mohtadi, M., and Hebbeln, D. (2004), Mechanisms and variations of the paleoproductivity off northern Chile (24°S–33°S) during the last 40,000 years, *Paleoceanography*, *19*(2).

Mohtadi, M., Oppo, D. W., Steinke, S., Stuut, J.-B. W., De Pol-Holz, R., Hebbeln, D., and Lückge, A. (2011), Glacial to Holocene swings of the Australian–Indonesian

monsoon, *Nature Geoscience*, *4*(8), 540-544.

Mohtadi, M., Lückge, A., Steinke, S., Permana, H., Susilohadi, S., Zuraida, R., and Jennerjahn, T. C. (2022), 9 - Late quaternary environmental history of Indonesia, in *Science for the Protection of Indonesian Coastal Ecosystems (SPICE)*, edited by T. C. Jennerjahn, T. Rixen, H. E. Irianto and J. Samiaji, pp. 347-369 Elsevier.

Neale, R., and Slingo, J. (2003), The Maritime Continent and Its Role in the Global Climate: A GCM Study, *Journal of Climate*, *16*(5), 834-848.

Nearing, M. A., et al. (2005), Modeling response of soil erosion and runoff to changes in precipitation and cover, *Catena*, *61*(2-3), 131-154.

Otto-Bliesner, B. L., Brady, E. C., Clauzet, G., Tomas, R., Levis, S., and Kothavala, Z. (2006), Last Glacial Maximum and Holocene Climate in CCSM3, *Journal of Climate*, *19*(11), 2526-2544.

Paterson, G. A., and Heslop, D. (2015), New methods for unmixing sediment grain size data, *Geochemistry, Geophysics, Geosystems*, *16*(12), 4494-4506.

Pena, L. D., Cacho, I., Ferretti, P., and Hall, M. A. (2008), El Niño-Southern Oscillation-like variability during glacial terminations and interlatitudinal teleconnections, *Paleoceanography*, *23*(3), n/a-n/a.

Peng, N., Dang, H., Wu, J., Aiello, I. W., and Jian, Z. (2021), Tectonic and climatic controls on the Plio-Pleistocene evolution of sediment discharge from Papua New Guinea, *Marine Geology*, *441*, 106627.

Petchey, F., and Ulm, S. (2016), Marine Reservoir Variation in the Bismarck Region: An Evaluation of Spatial and Temporal Change in ΔR and R Over the Last 3000 Years, *Radiocarbon*, *54*(1), 45-58.

Philander, S. G. H., Gu, D., Lambert, G., Li, T., Halpern, D., Lau, N. C., and Pacanowski, R. C. (1996), Why the ITCZ Is Mostly North of the Equator, *Journal of Climate*, *9*(12), 2958-2972.

Pico, T., McGee, D., Russell, J., and Mitrovica, J. X. (2020), Recent Constraints on MIS 3 Sea Level Support Role of Continental Shelf Exposure as a Control on Indo-Pacific Hydroclimate, *Paleoceanography and Paleoclimatology*, *35*(8), e2020PA003998.

Prins, M. A., and Weltje, G. J. (1999), End-member modeling of siliciclastic grain-size distributions: The late Quaternary record of eolian and fluvial sediment supply to the Arabian Sea and its paleoclimatic significance, edited, pp. 91 - 111.

Raddatz, J., Nürnberg, D., Tiedemann, R., and Rippert, N. (2017), Southeastern marginal West Pacific Warm Pool sea-surface and thermocline dynamics during the Pleistocene (2.5–0.5 Ma), *Palaeogeography, Palaeoclimatology, Palaeoecology*, *471*, 144-156.

Rafter, P. A., and Charles, C. D. (2012), Pleistocene equatorial Pacific dynamics inferred from the zonal asymmetry in sedimentary nitrogen isotopes, *Paleoceanography*, *27*(3).

Rea, D. K., Hovan, S. A., and Janecek, T. R. (1994), Late Quaternary Flux of Eolian Dust to the Pelagic Ocean, in *Material Fluxes on the Surface of the Earth*, edited

by W. W. Hay, The National Academies Press, Washington, DC.

Russell, J. M., Vogel, H., Konecky, B. L., Bijaksana, S., Huang, Y., Melles, M., Wattrus, N., Costa, K., and King, J. W. (2014), Glacial forcing of central Indonesian hydroclimate since 60,000 y B.P, *Proceedings of the National Academy of Sciences*, *111*(14), 5100-5105.

Sardeshmukh, P. D., and Hoskins, B. J. (1988), The Generation of Global Rotational Flow by Steady Idealized Tropical Divergence, *Journal of the Atmospheric Sciences*, *45*(7), 1228-1251.

Schmidt, M. W., and Spero, H. J. (2011), Meridional shifts in the marine ITCZ and the tropical hydrologic cycle over the last three glacial cycles, *Paleoceanography*, *26*(1), PA1206.

Scroxton, N., Burns, S. J., McGee, D., Hardt, B., Godfrey, L. R., Ranivoharimanana, L., and Faina, P. (2017), Hemispherically in-phase precipitation variability over the last 1700 years in a Madagascar speleothem record, *Quaternary Science Reviews*, *164*, 25-36.

Selvaraj, K., and Chen, C. Tung A. (2006), Moderate Chemical Weathering of Subtropical Taiwan: Constraints from Solid - Phase Geochemistry of Sediments and Sedimentary Rocks, *The Journal of Geology*, *114*(1), 101-116.

Shen, Z., Conway, N., and Hanebuth, T. J. J. (2021), A novel binary pipette splitting sediment subsampling method for improving reproducibility in laser-diffraction particle-size analysis, *MethodsX*, *8*, 101493.

Shiau, L.-J., Chen, M.-T., Huh, C.-A., Yamamoto, M., and Yokoyama, Y. (2012), Insolation and cross-hemispheric controls on Australian monsoon variability over the past 180 ka: new evidence from offshore southeastern Papua New Guinea, *Journal of Quaternary Science*, *27*(9), 911-920 %U https://doi.org/910.1002/jqs.2581.

Singarayer, J. S., Valdes, P. J., and Roberts, W. H. G. (2017), Ocean dominated expansion and contraction of the late Quaternary tropical rainbelt, *Scientific Reports*, *7*(1), 9382.

Stott, L., Poulsen, C., Lund, S., and Thunell, R. (2002), Super ENSO and global climate oscillations at millennial time scales, *Science (New York, N.Y.)*, *297*, 222-226.

Tachikawa, K., Cartapanis, O., Vidal, L., Beaufort, L., Barlyaeva, T., and Bard, E. (2011), The precession phase of hydrological variability in the Western Pacific Warm Pool during the past 400 ka, *Quaternary Science Reviews*, *30*(25-26), 3716-3727.

Timmermann, A., Lorenz, S. J., An, S. I., Clement, A., and Xie, S. P. (2007), The Effect of Orbital Forcing on the Mean Climate and Variability of the Tropical Pacific, *Journal of Climate*, *20*(16), 4147-4159.

Waelbroecka, C., Labeyriea, L., Michela, E., Duplessya, J. C., McManusc, J. F., Lambeckd, K., Balbona, E., and Labracheriee, M. (2002), Sea-level and deep water temperature changes derived from benthic foraminifera isotopic records,

Quaternary Science Reviews, *21*, 11.

Wan, S., Sun, Y., and Nagashima, K. (2020), Asian dust from land to sea: processes, history and effect from modern observation to geological records, *Geological Magazine*, *157*(5), 701-706.

Wan, S., Li, A., Jan-Berend, W. S., and Xu, F. (2007), Grain-size records at ODP site 1146 from the northern South China Sea: Implications on the East Asian monsoon evolution since 20 Ma, *Science in China Series D: Earth Sciences*, *50*(10), 1536-1547.

Wan, S., Yu, Z., Clift, P. D., Sun, H., Li, A., and Li, T. (2012), History of Asian eolian input to the West Philippine Sea over the last one million years, *Palaeogeography, Palaeoclimatology, Palaeoecology*, *326-328*, 152-159.

Wan, S., et al. (2015), Human impact overwhelms long-term climate control of weathering and erosion in southwest China, *Geology*, *43*(5), 439-442.

Wang, B., and Ding, Q. (2008), Global monsoon: Dominant mode of annual variation in the tropics, *Dynamics of Atmospheres and Oceans*, *44*(3-4), 165-183.

Wang, C. (2019), Three-ocean interactions and climate variability: a review and perspective, *Climate Dynamics*, *53*(7-8), 5119-5136.

Wang, P. (2021), Low-latitude forcing: A new insight into paleo-climate changes, *The Innovation*, *2*(3), 100145.

Wang, R.-M., You, C.-F., Chung, C.-H., Huang, K.-F., and Hsu, Y.-J. (2022), Uranium isotopes in a subtropical mountainous river of Taiwan: Insight into physical and chemical weathering processes, *Journal of Hydrology*, *607*, 127481.

West, A. J. (2012), Thickness of the chemical weathering zone and implications for erosional and climatic drivers of weathering and for carbon-cycle feedbacks, *Geology*, *40*(9), 811-814.

Windler, G., Tierney, J. E., and Anchukaitis, K. J. (2021), Glacial‐Interglacial Shifts Dominate Tropical Indo‐Pacific Hydroclimate During the Late Pleistocene, *Geophysical Research Letters*, *48*(15), e2021GL093339.

Windler, G., Tierney, J. E., DiNezio, P. N., Gibson, K., and Thunell, R. (2019), Shelf exposure influence on Indo-Pacific Warm Pool climate for the last 450,000 years, *Earth and Planetary Science Letters*, *516*, 66-76.

Wu, J., Liu, Z., and Zhou, C. (2012), Late Quaternary glacial cycle and precessional period of clay mineral assemblages in the Western Pacific Warm Pool, Chinese Science Bulletin, 57(28-29), 3748-3760.

Wu, J., Zhang, L., Wang, F., Kaluwin, C., and Hu, D. (2022), Currents off the Papua New Guinea Coast During and After the El Niño of 2015–2016, *Journal of Geophysical Research: Oceans*, *127*(12), e2022JC018760 %U https://onlinelibrary.wiley.com/doi/abs/018710.011029/012022JC018760.

Wu, Q., Colin, C., Liu, Z., Bassinot, F., Dubois-Dauphin, Q., Douville, E., Thil, F., and Siani, G. (2017), Foraminiferal εNd in the deep north-western subtropical Pacific Ocean: Tracing changes in weathering input over the last 30,000 years, *Chemical Geology*, *470*, 55-66.

Xiao, S., Li, A., Liu, J. P., Chen, M., Xie, Q., Jiang, F., Li, T., Xiang, R., and Chen, Z. (2006), Coherence between solar activity and the East Asian winter monsoon variability in the past 8000 years from Yangtze River-derived mud in the East China Sea, *Palaeogeography, Palaeoclimatology, Palaeoecology*, *237*(2-4), 293-304.

Xiong, Z., et al. (2018), Rapid precipitation changes in the tropical West Pacific linked to North Atlantic climate forcing during the last deglaciation, *Quaternary Science Reviews*, *197*, 288-306.

Yan, H., Wei, W., Soon, W., An, Z., Zhou, W., Liu, Z., Wang, Y., and Carter, R. M. (2015), Dynamics of the intertropical convergence zone over the western Pacific during the Little Ice Age, *Nature Geoscience*, *8*(4), 315-320.

Yeager, S. G., Shields, C. A., Large, W. G., and Hack, J. J. (2006), The Low-Resolution CCSM3, *Journal of Climate*, *19*(11), 2545-2566.

Yu, Z., Wan, S., Colin, C., Song, L., Zhao, D., Huang, J., Sun, H., Xu, Z., Li, A., and Li, T. (2018), ENSO-Like Modulated Tropical Pacific Climate Changes Since 2.36 Myr and Its Implication for the Middle Pleistocene Transition, *Geochemistry, Geophysics, Geosystems*, *19*(2), 415-426.

Yu, Z., Tang, X., Colin, C., Wilson, D. J., Zhou, X., Song, L., Chang, F., Zhang, S., Bassinot, F., and Wan, S. (2023), Millennial-Scale Precipitation Variability in the Indo-Pacific Region Over the Last 40 Kyr, *Geophysical Research Letters*, *50*(2), e2022GL101646.

Yu, Z., et al. (2016), Co-evolution of monsoonal precipitation in East Asia and the tropical Pacific ENSO system since 2.36 Ma: New insights from high-resolution clay mineral records in the West Philippine Sea, *Earth and Planetary Science Letters*, *446*, 45-55.

Yu, Z., et al. (2019), Sea level-controlled sediment transport to the eastern Arabian Sea over the past 600 kyr: Clay minerals and SrNd isotopic evidence from IODP site U1457, *Quaternary Science Reviews*, *205*, 22-34 %U https://www.sciencedirect.com/science/article/pii/S0277379118305663.

Zenk, W., Siedler, G., Ishida, A., Holfort, J., Kashino, Y., Kuroda, Y., Miyama, T., and Müller, T. J. (2005), Pathways and variability of the Antarctic Intermediate Water in the western equatorial Pacific Ocean, *Progress in Oceanography*, *67*(1), 245-281.

Zhang, L., Wu, J., Wang, F., Hu, S., Wang, Q., Jia, F., Wang, F., and Hu, D. (2020a), Seasonal and Interannual Variability of the Currents off the New Guinea Coast From Mooring Measurements, *Journal of Geophysical Research: Oceans*, *125*(12), e2020JC016242 %U https://onlinelibrary.wiley.com/doi/abs/016210.011029/012020JC016242.

Zhang, P., Xu, J., Holbourn, A., Kuhnt, W., Xiong, Z., and Li, T. (2022), Obliquity Induced Latitudinal Migration of the Intertropical Convergence Zone During the Past ~410 kyr, *Geophysical Research Letters*, *49*(21), e2022GL100039 %U https://onlinelibrary.wiley.com/doi/abs/100010.101029/102022GL100039.

Zhang, P., et al. (2020b), Indo‐Pacific Hydroclimate in Response to Changes of the Intertropical Convergence Zone: Discrepancy on Precession and Obliquity Bands Over the Last 410 kyr, *Journal of Geophysical Research: Atmospheres*, *125*(14), e2019JD032125.

Zhang, S., Li, T., Chang, F., Yu, Z., Xiong, Z., and Wang, H. (2016), Correspondence between the ENSO-like state and glacial-interglacial condition during the past 360 kyr, *Chinese Journal of Oceanology and Limnology*, *35*(5), 1018-1031.

Zhang, S., Yu, Z., Gong, X., Wang, Y., Chang, F., Lohmman, G., Qi, Y., and Li, T. (2021), Precession cycles of the El Niño/Southern oscillation-like system controlled by Pacific upper-ocean stratification, *Communications Earth & Environment*, *2*(2021), 239.

Zhang, Y., Xu, J., Li, G., Lu, Z., Jiang, Z., Zhang, W., and Liu, Y. (2023), ENSO-like evolution of the tropical Pacific climate mean state and its potential causes since 300ka, *Quaternary Science Reviews*, *315*, 108241.

Zhao, D., Wan, S., Lu, Z., Zhai, L., Feng, X., Shi, X., and Li, A. (2020), Response of heterogeneous rainfall variability in East Asia to Hadley circulation reorganization during the late Quaternary, *Quaternary Science Reviews*, *247*, 106562 %U https://www.sciencedirect.com/science/article/pii/S0277379120305242.

Declaration of interests

☒The authors declare that they have no known competing financial interests or personal relationships that could have appeared to influence the work reported in this paper.

☐The authors declare the following financial interests/personal relationships which may be considered as potential competing interests:

Highlights:

(1) First high temporal resolution grain size record of sediment dynamics in Tropical Western Pacific islands

(2) This grain size record exhibits precessional changes in phase with modelled ENSO variations

(3) Precipitation and atmospheric convection in the WPWP are likely controlled by ENSO-like conditions, while the ITCZ impacts larger spatial precipitation anomalies

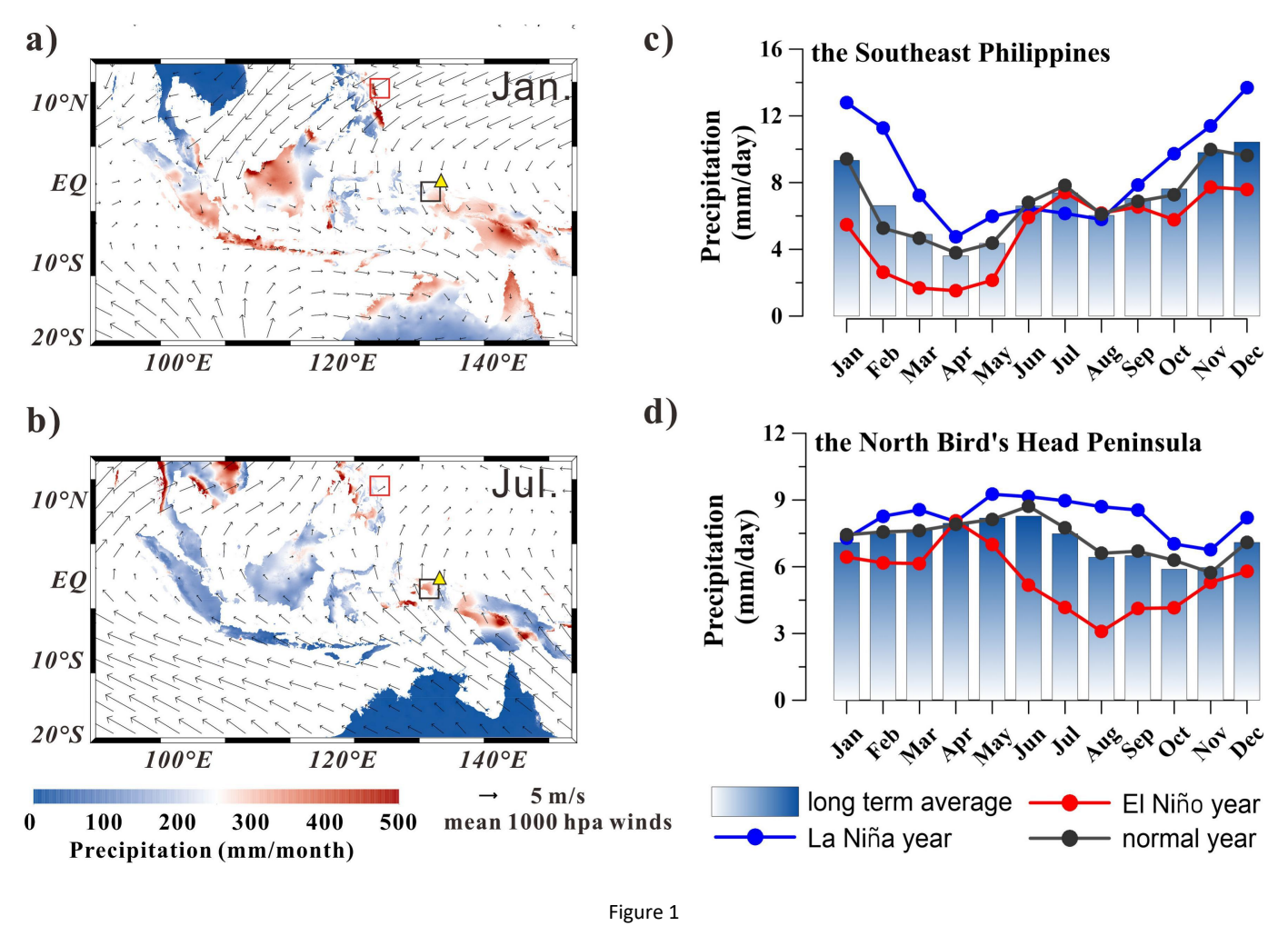
a)
Jan.
10°N
EQ
10°S
20°S
100°E
120°E
140°E
b)
Jul.
10°N
EQ
10°S
20°S
100°E
120°E
140°E
0
100
200
300
400
500
Precipitation (mm/month)
5 m/s
mean 1000 hpa winds
c)
the Southeast Philippines
Precipitation (mm/day)
16
12
8
4
0
Jan
Feb
Mar
Apr
May
Jun
Jul
Aug
Sep
Oct
Nov
Dec
d)
the North Bird's Head Peninsula
Precipitation (mm/day)
12
9
6
3
0
Jan
Feb
Mar
Apr
May
Jun
Jul
Aug
Sep
Oct
Nov
Dec
long term average
El Niño year
La Niña year
normal year

Figure 1

a)

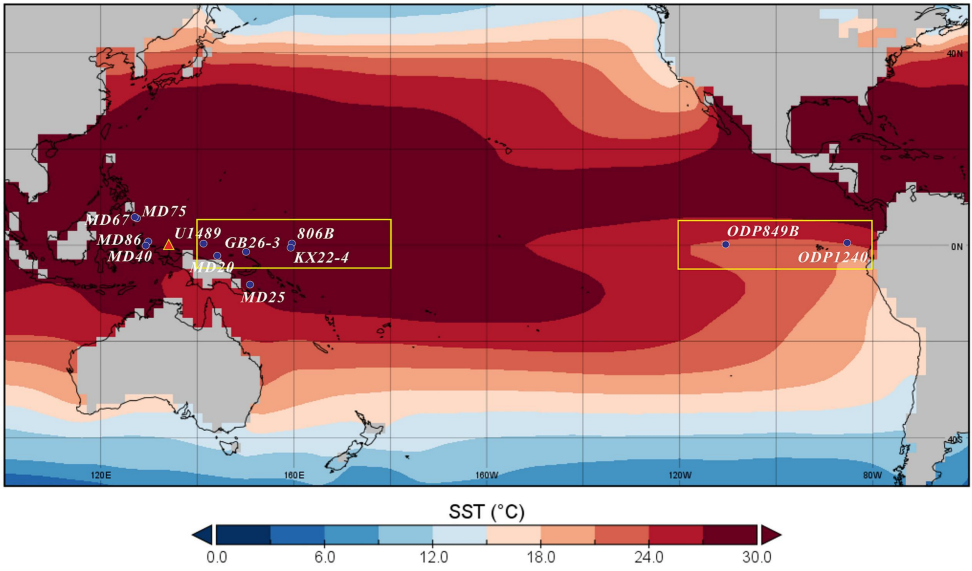
MD67
MD75
MD86
MD40
U1489
GB26-3
806B
KX22-4
MD20
MD25
ODP849B
ODP1240
40N
0N
40S
120E
160E
160W
120W
80W
SST (°C)
0.0
6.0
12.0
18.0
24.0
30.0

b)

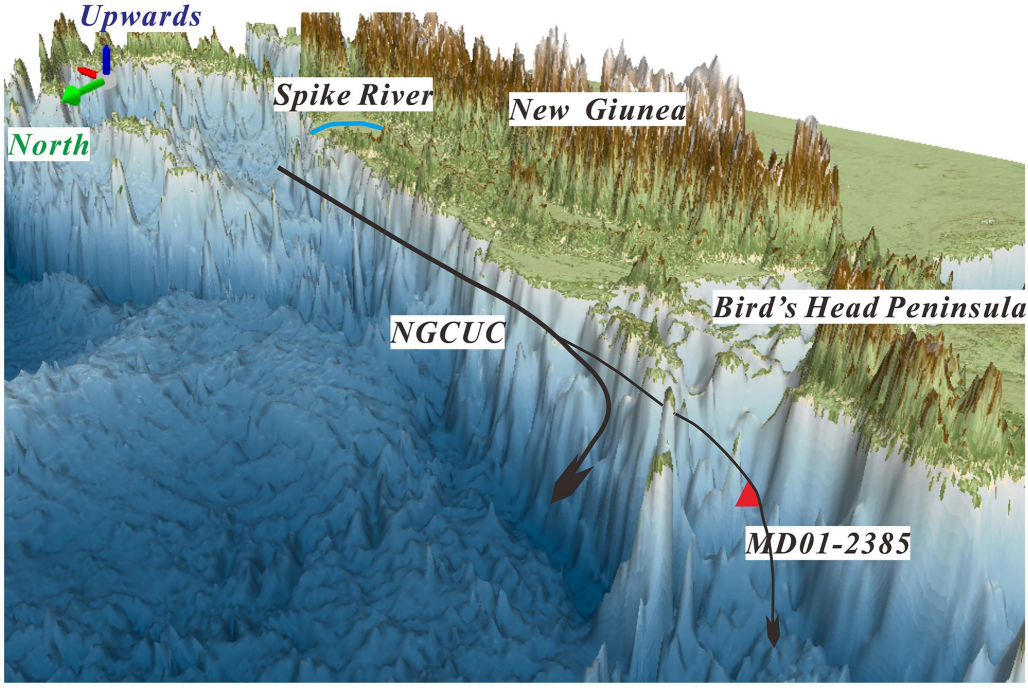
Upwards
North
Spike River
New Giunea
NGCUC
Bird's Head Peninsula
MD01-2385

Figure 2

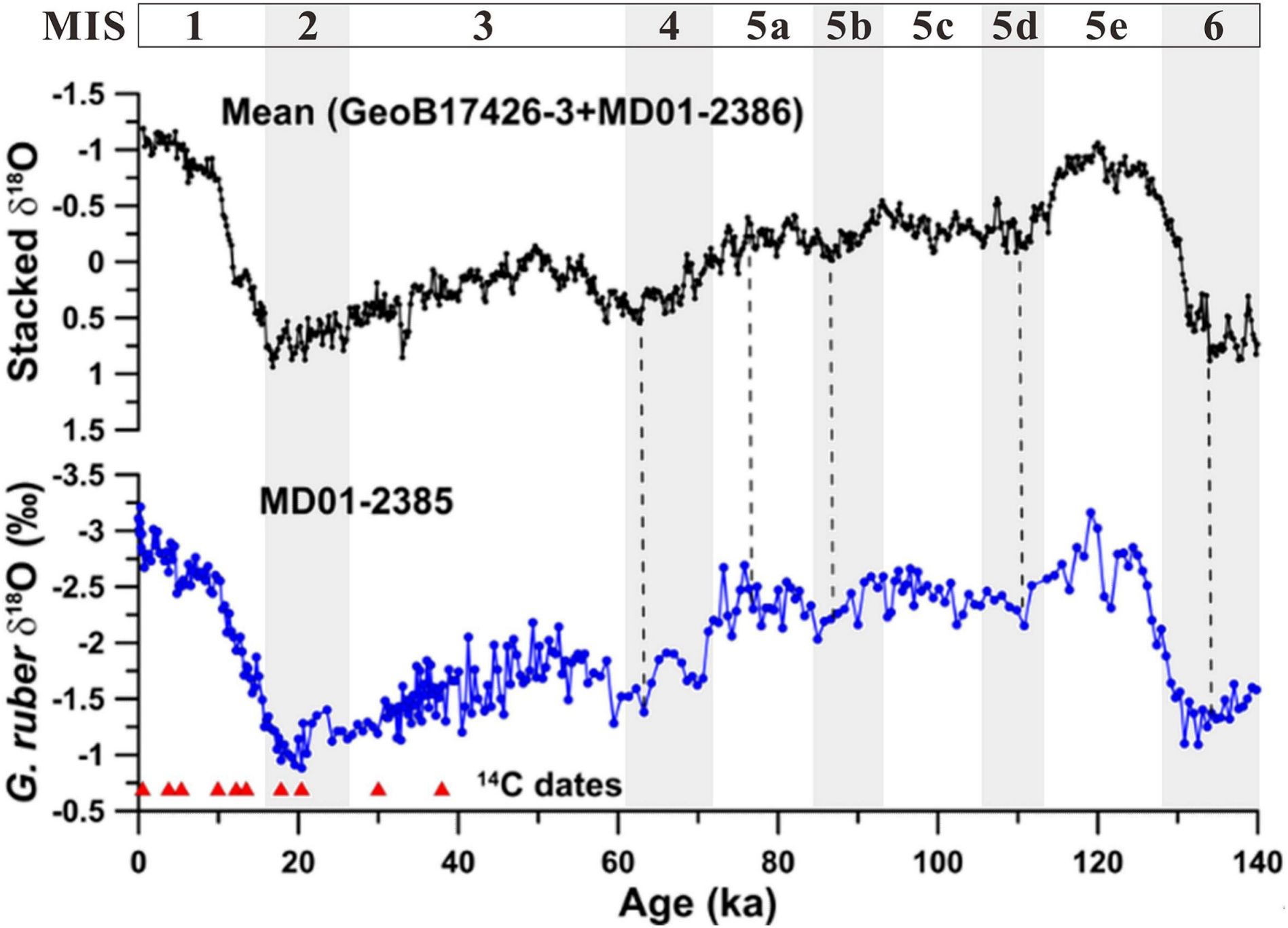
MIS
1
2
3
4
5a
5b
5c
5d
5e
6
Mean (GeoB17426-3+MD01-2386)
Stacked δ18O
-1.5
-1
-0.5
0
0.5
1
1.5
MD01-2385
G. ruber δ18O (‰)
-3.5
-3
-2.5
-2
-1.5
-1
-0.5
14C dates
0
20
40
60
80
100
120
140
Age (ka)

Figure 3

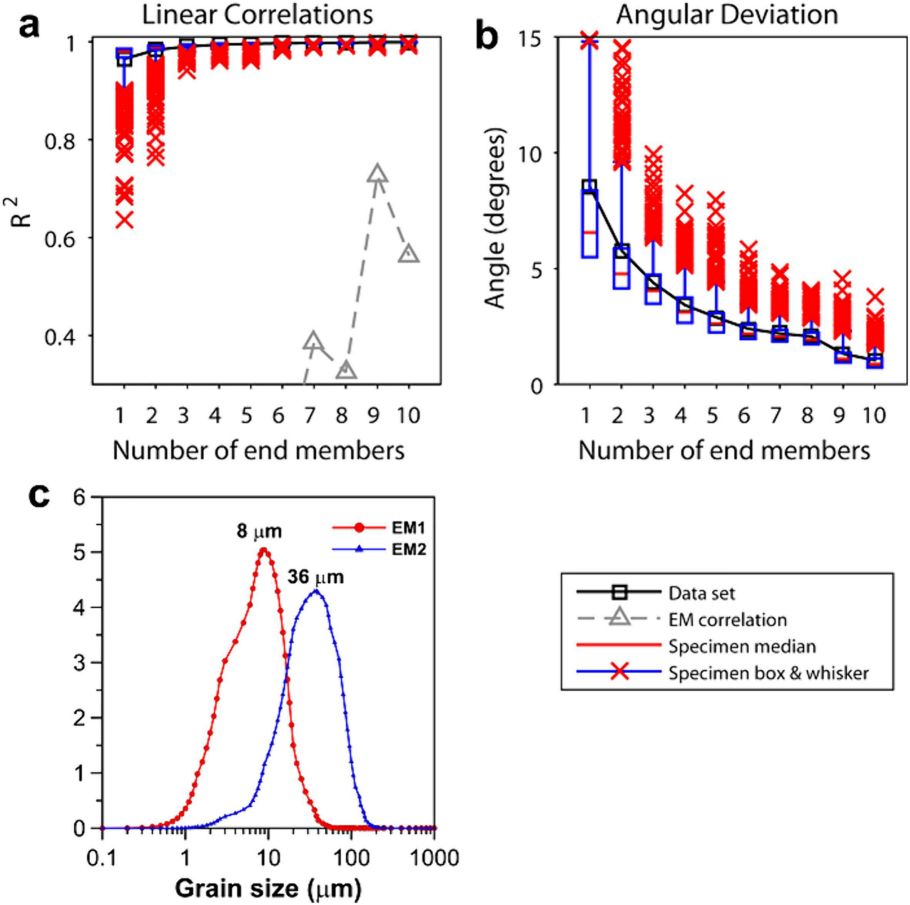
a
Linear Correlations
R 2
Number of end members
b
Angular Deviation
Angle (degrees)
Number of end members
c
8 μm
36 μm
EM1
EM2
Grain size (μm)
Data set
EM correlation
Specimen median
Specimen box & whisker

Figure 4

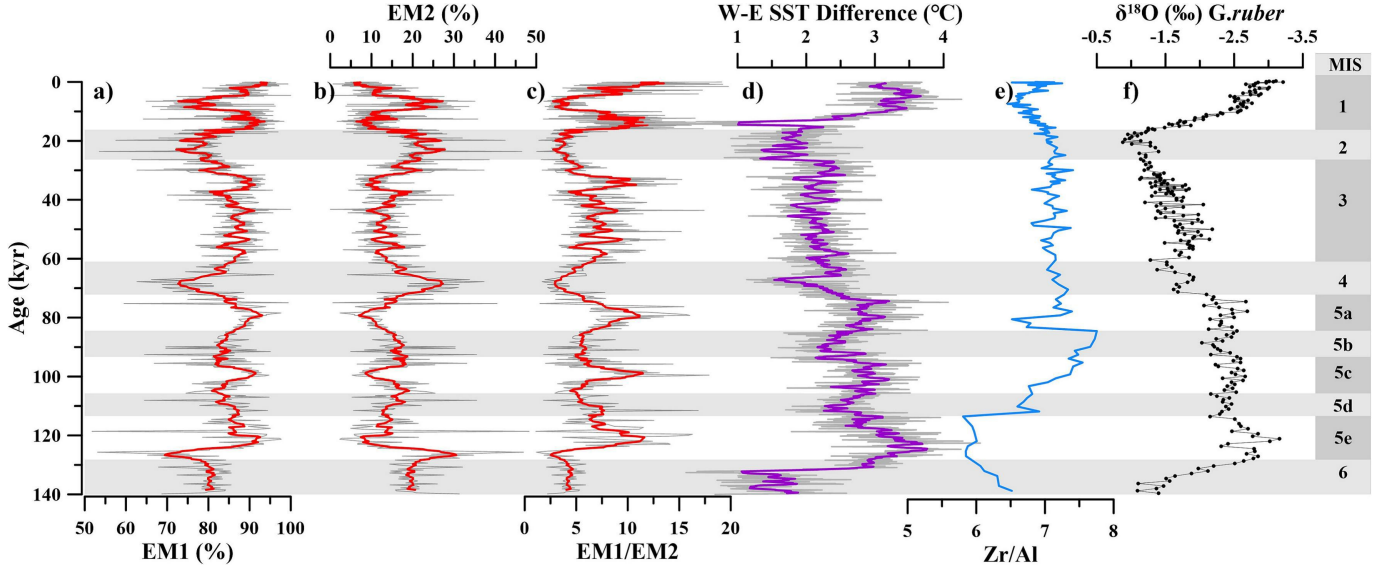
EM2 (%)
0 10 20 30 40 50
W-E SST Difference (°C)
1 2 3 4
δ18O (‰) G.ruber
-0.5 -1.5 -2.5 -3.5
MIS
1
2
3
4
5a
5b
5c
5d
5e
6
a)
b)
c)
d)
e)
f)
Age (kyr)
0 20 40 60 80 100 120 140
50 60 70 80 90 100
EM1 (%)
0 5 10 15 20
EM1/EM2
5 6 7 8
Zr/Al

Figure 5

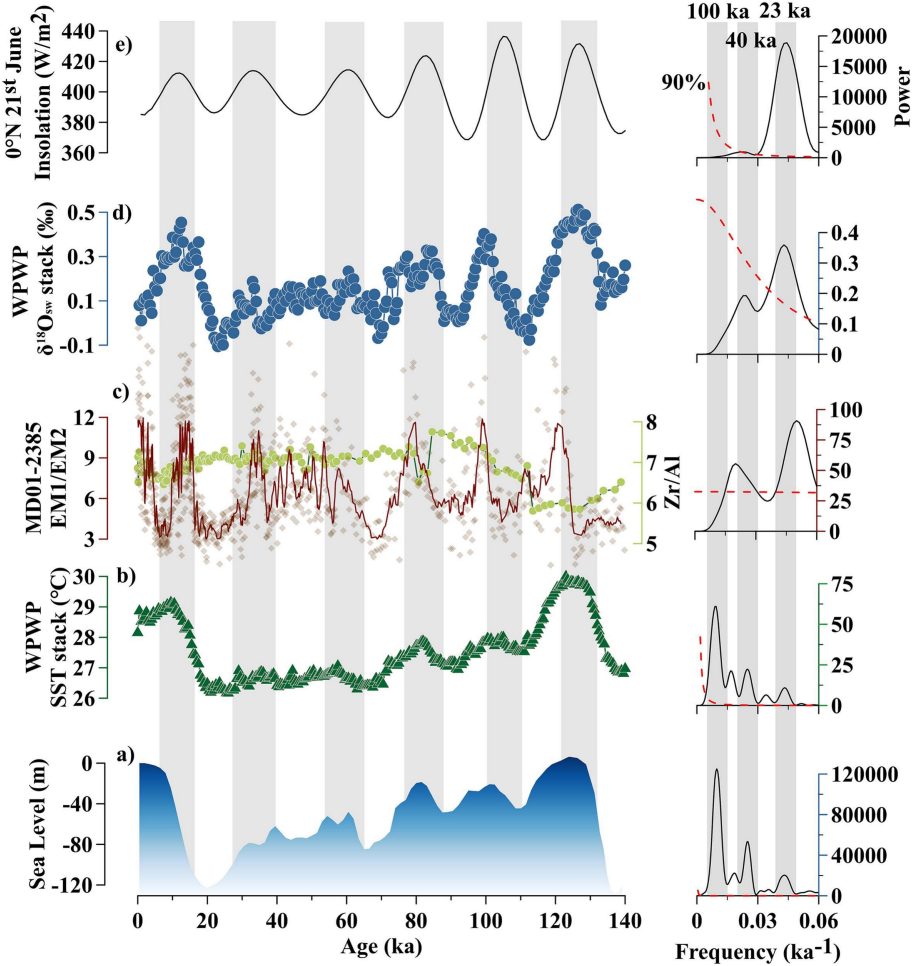
e)
0°N 21st June Insolation (W/m2)
440
420
400
380
360
d)
WPWP δ18Osw stack (‰)
0.5
0.3
0.1
-0.1
c)
MD01-2385 EM1/EM2
12
9
6
3
Zr/Al
8
7
6
5
b)
WPWP SST stack (°C)
30
29
28
27
26
a)
Sea Level (m)
0
-40
-80
-120
0
20
40
60
80
100
120
140
Age (ka)
100 ka
23 ka
40 ka
90%
Power
20000
15000
10000
5000
0
0.4
0.3
0.2
0.1
0
100
75
50
25
0
75
50
25
0
120000
80000
40000
0
0
0.03
0.06
Frequency (ka-1)

Figure 6

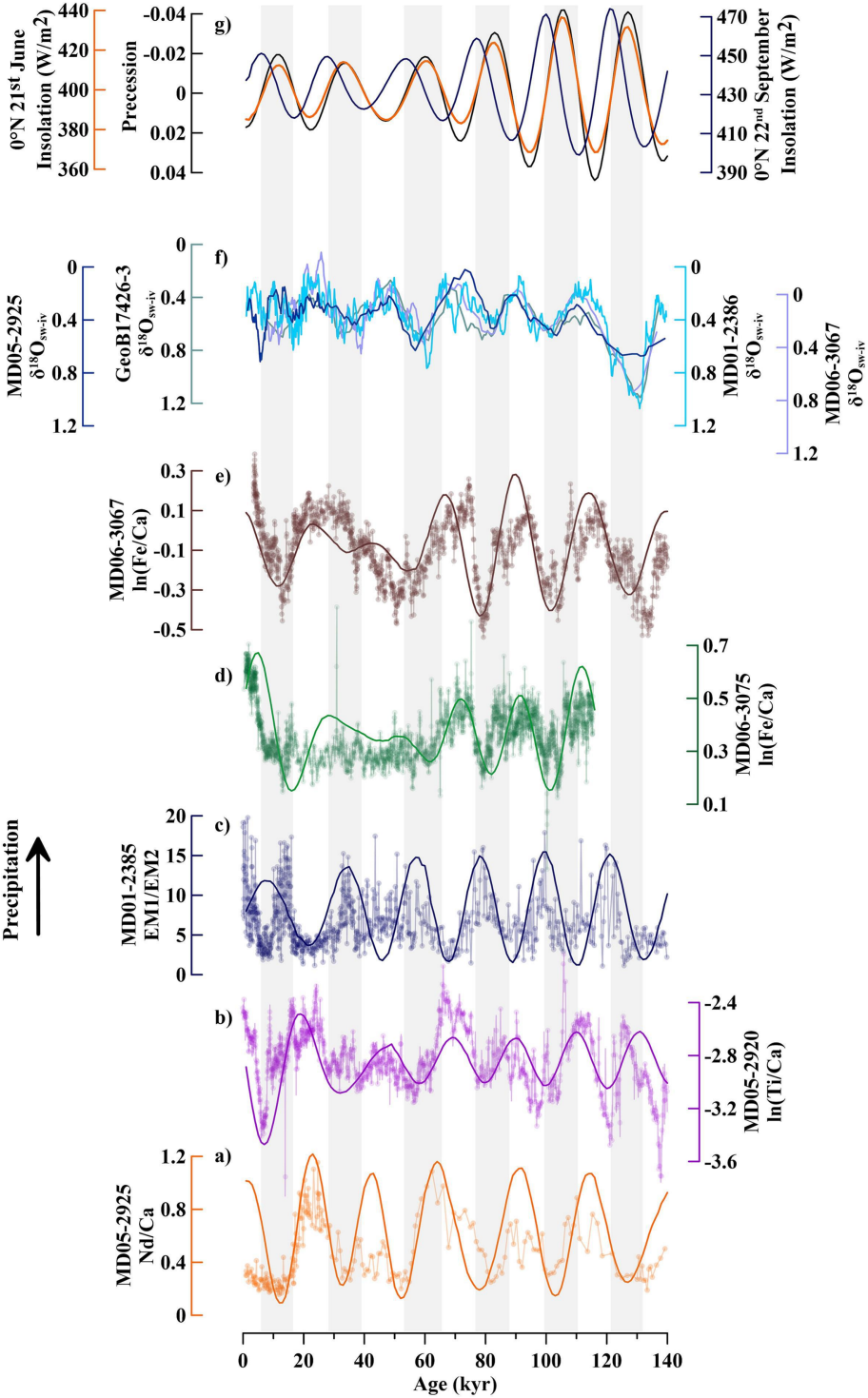
0°N 21st June Insolation (W/m2)
440
420
400
380
360
Precession
-0.04
-0.02
0
0.02
0.04
g)
0°N 22nd September Insolation (W/m2)
470
450
430
410
390
MD05-2925 δ18Osw-iv
GeoB17426-3 δ18Osw-iv
f)
MD01-2386 δ18Osw-iv
MD06-3067 δ18Osw-iv
0
0.4
0.8
1.2
MD06-3067 ln(Fe/Ca)
0.3
0.1
-0.1
-0.3
-0.5
e)
d)
MD06-3075 ln(Fe/Ca)
0.7
0.5
0.3
0.1
Precipitation
MD01-2385 EM1/EM2
20
15
10
5
0
c)
b)
MD05-2920 ln(Ti/Ca)
-2.4
-2.8
-3.2
-3.6
MD05-2925 Nd/Ca
1.2
0.8
0.4
0
a)
0
20
40
60
80
100
120
140
Age (kyr)

Figure 7

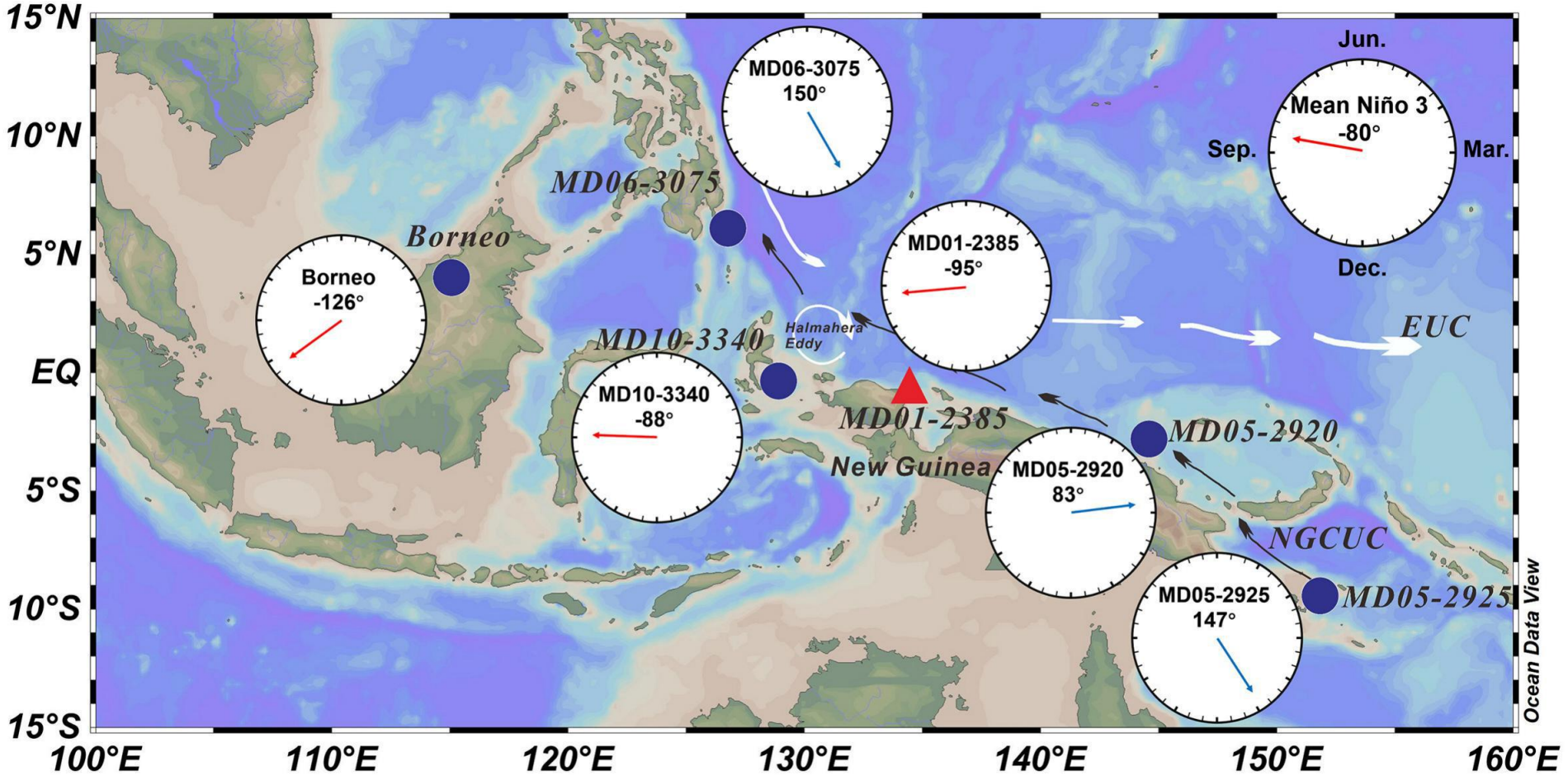
15°N
10°N
5°N
EQ
5°S
10°S
15°S
100°E
110°E
120°E
130°E
140°E
150°E
160°E
MD06-3075
150°
MD06-3075
Borneo
Borneo
-126°
MD01-2385
-95°
Jun.
Mean Niño 3
-80°
Sep.
Mar.
Dec.
EUC
MD10-3340
Halmahera
Eddy
MD10-3340
-88°
MD01-2385
MD05-2920
New Guinea
MD05-2920
83°
NGCUC
MD05-2925
147°
MD05-2925
Ocean Data View

Figure 8

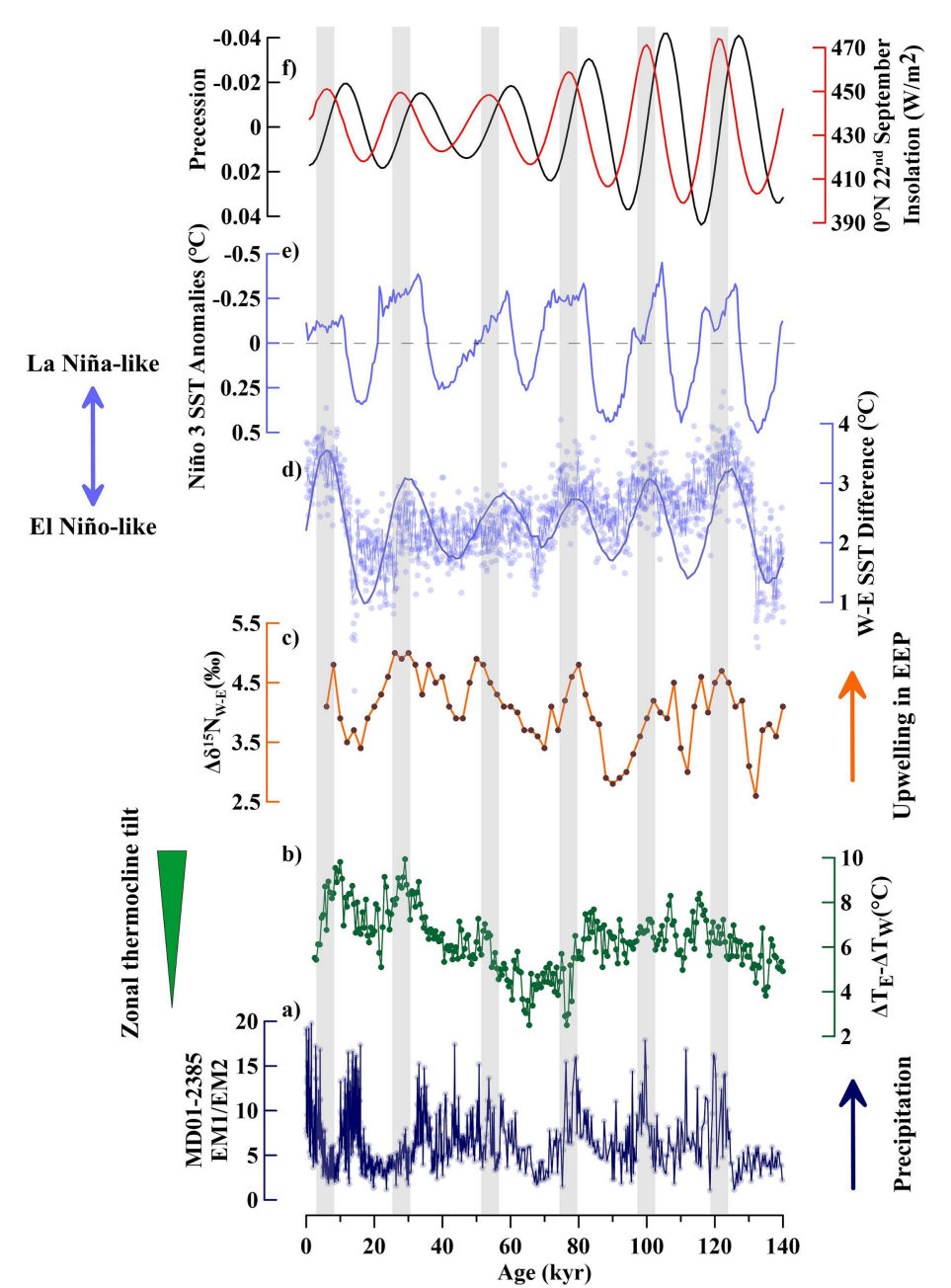
f)
Precession
-0.04
-0.02
0
0.02
0.04
470
450
430
410
390
0°N 22nd September Insolation (W/m2)
e)
Niño 3 SST Anomalies (°C)
-0.5
-0.25
0
0.25
0.5
La Niña-like
El Niño-like
d)
4
3
2
1
W-E SST Difference (°C)
c)
5.5
4.5
3.5
2.5
Δδ15NW-E (‰)
Upwelling in EEP
Zonal thermocline tilt
b)
10
8
6
4
2
ΔTE-ΔTW(°C)
a)
20
15
10
5
0
MD01-2385
EM1/EM2
Precipitation
0
20
40
60
80
100
120
140
Age (kyr)

Figure 9

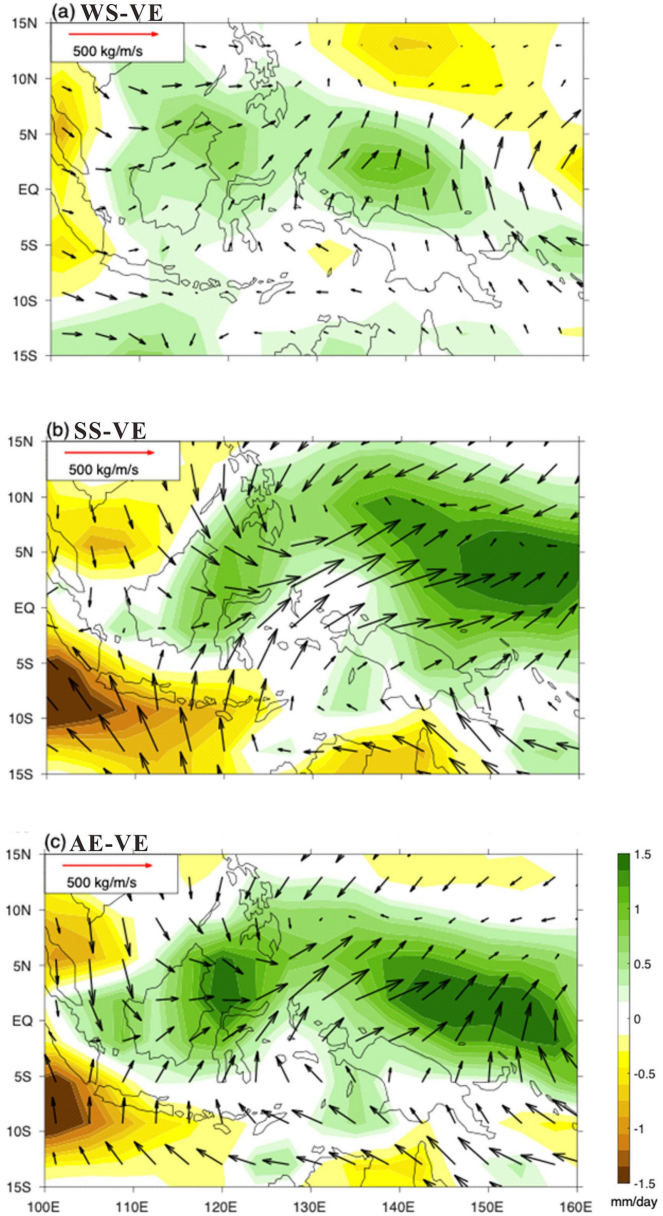
(a) WS-VE
500 kg/m/s
(b) SS-VE
500 kg/m/s
(c) AE-VE
500 kg/m/s
15N
10N
5N
EQ
5S
10S
15S
100E
110E
120E
130E
140E
150E
160E
1.5
1
0.5
0
-0.5
-1
-1.5
mm/day

Figure 10